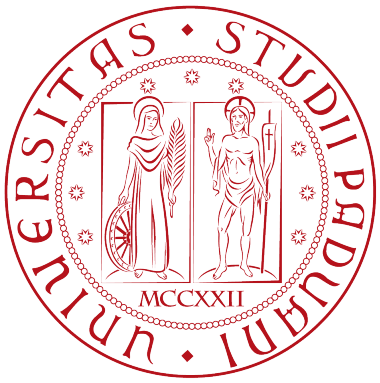

Università degli Studi di Padova

Dipartimento di Fisica e Astronomia "Galileo Galilei"
Master Degree in Astrophysics and Cosmology

Final Dissertation

Constraining the composition of pristine material through first-generation stars in globular clusters

Thesis supervisor:
Prof. Antonino P. Milone
Thesis co-supervisor:
Dr. Edoardo P. Lagioia

Candidate:
Maria Vittoria Legnardi

Academic Year 2020/21

Abstract

Nearly all Globular Clusters (GCs) host multiple stellar populations (MPs), including a first population (1G) with the same content of light elements as halo field stars at similar metallicity and one or more second populations (2G) of stars enhanced in He, N and Na, and depleted in C and O. 1G stars, in particular, reflect the chemical composition of the pristine material from which GCs formed and are considered by far chemically homogeneous.
The long-held hypothesis of chemical homogeneity in 1G stars has been recently challenged by studies based on the 'Chromosome Map' (ChM), a photometric diagram exquisitely sensitive to variations in C, N, O and helium between GC stars. Since these works are based on evolved red giant branch (RGB) stars, two main possibilities could explain this unexpected discovery: star-to-star chemical variations due to stellar evolution or small scale inhomogeneities in the pristine material from which GCs formed at high redshift.
To disentangle between the two scenarios, I performed a detailed study of the MP composition of main sequence (MS) stars of the Galactic GC NGC 6362 by using high precision multi-band photometry from the Hubble Space Telescope (HST). Specifically, I first build the ChM for unevolved stars and then I compared the observed colors with the ones inferred from grids of synthetic spectra with appropriate chemical compositions. In close analogy to what was already observed for the RGB stars of this cluster, the ChM analysis revealed chemical inhomogeneities among the cluster 1G MS stars. Moreover, from the comparison with synthetic spectra I found that the 1G component has constant C, N, O content but exhibits significant star-to-star variations either in helium or iron. In contrast, 2G stars of NGC 6362 exhibit negligible internal chemical variations.
My discovery that chemical variations are present among unevolved MS 1G stars, rules out the possibility that chemical inhomogeneities are the result of stellar evolution. Hence, 1G stars are tracers of the chemical composition of the primordial cloud where they formed at high redshift.
In light of these findings, I exploited the colors of 1G RGB stars to infer the maximum abundance spread within the 1G of 55 Galactic GCs. Additionally, I investigated the relations between the elemental spread and the main parameters of the host GC. From this analysis I found that the maximum metallicity variation ranges from [Fe/H] $\sim$ 0.0 to [Fe/H] $\sim$ 0.3 dex and correlates both with GC mass and the 1G mass. I derived similar correlations by assuming that the color spread of 1G stars is due to helium variation. Intriguingly, the 1G stars of those GCs with the red horizontal branch (HB; M 3-like) exhibit wider abundance scatter than in GCs with the blue-HB alone (M 13-like). Moreover, only M 3-like GCs exhibit the correlation between internal iron and helium variations and cluster mass.
The results of this thesis are used to qualitatively constrain the environment where the proto-GCs formed in the early Universe. I also speculated possible implications on the formation of 2G stars within GCs and on the second-parameter phenomenon of the HB morphology.

Contents

Chapter 1

Introduction

Nowadays, globular clusters (GCs) are considered complex systems composed by multiple stellar populations (MPs) with different chemical composition. The aim of this Chapter is to present the modern view of such objects and introduce the main tools that have allowed to revisit the description of GCs in the past few years.
Specifically, Section 1.1 illustrates the mostly used photometric diagrams to identify MPs. Section 1.2 and 1.3, instead, summarize respectively the main observational properties of MPs and the scenarios suggested to explain their formation in GCs. Then, Section 1.4 presents the main phenomenon investigated in this work introducing possible explanations proposed so far by different authors in order to interpret it. Finally, Section 1.5 describes the purpose and the outline of this thesis.

1.1 Multiple Populations in Globular Clusters

Until a few years ago GCs were considered the prototypes of simple stellar populations (SSPs), composed of coeval stars with the same chemical composition. Indeed, their color-magnitude diagrams (CMDs), including those obtained from high-precision Hubble Space Telescope (HST) photometry, were similar to single isochrones, like the one shown in Figure 1.1 for NGC 5272 (M 3). The modern view of a GC is, however, much more complex that the one depicted by this kind of CMD: indeed, it is now widely accepted that nearly all GCs are composed of MPs, namely discrete groups of stars with different light-element (C, N, O, Al, Mg) and helium contents. MPs correspond to distinct sequences in CMDs that can be followed continuously at all evolutionary stages, from the bottom of the main sequence (MS) up to the tip of the red giant branch (RGB), in the horizontal branch (HB) and in the asymptotic giant branch (AGB).
One of the most important factors that led to the discovery of MPs is the availability of improved techniques for the reduction of HST photometric data based on the effective point-spread function (ePSF; Section 2.3) introduced by Jay Anderson and collaborators (Anderson and King, 2000). The ePSF allowed to achieve an accuracy in measuring positions and magnitudes of stars that was never reached before, thus making possible to identify and characterize MPs in a large sample of GCs.
Another fundamental ingredient to achieve this result was the introduction of new color combinations sensitive to chemical differences among stars. Examples

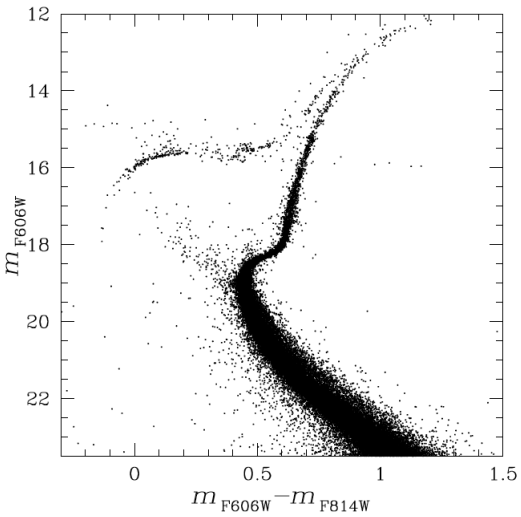

Figure 1.1: CMD of the galactic GC NGC 5272 (M 3) in the F606W and F814W filters of HST. Clearly, it is not possible to disentangle MPs in these optical bands. Figure from Anderson et al. (2008b).

of CMDs that exploit these color combinations are shown in Figure 1.2 and 1.3 where multiple sequences are clearly recognizable along all evolutionary stages. In particular, the photometric diagram of Figure 1.2 is built with a wide color baseline, $m_{F275W} - m_{F814W}$, crucial to retrieve variations of helium (He) abundance among stars. Also combinations of the three UVIS/WFC3 filters F275W, F336W and F438W, eventually substituted by other HST bands, including F225W, F343N or F410M, are extremely useful tools to identify MPs. Indeed, the passband of the previous filters encompass the absorption features of the OH, NH, CH and CN allowing to separate populations with different abundances in light-elements. This can be clearly observed in the photometric diagrams of Figure 1.3, built with different combinations of F275W, F336W and F410M bands. Specifically, in the $(m_{F336W} - m_{F410M})$ vs.$(m_{F275W} - m_{F336W})$ two-color diagrams of panels (a) and (b), stellar populations clearly define distinct sequences. These diagrams, however, allow to identify MPs only if different evolutionary stages are considered separately. To overcome this limitation, the pseudo-color $C_{F275W,F336W,F438W} = (m_{F275W} - m_{F336W}) - (m_{F336W} - m_{F438W})$ was then introduced (Milone et al., 2013): CMDs that exploit it, like the one shown in panel (c) of Figure 1.3 (the filter F438W is substituted by F410M), allow to characterize MPs in the entire range of available magnitudes.

All the photometric diagrams presented so far were instrumental to demonstrate that nearly all GCs host a first population (1G) composed of stars with the same content of light-elements as halo field stars at similar metallicity, and one or more second population (2G) of stars enhanced in He, nitrogen (N) and sodium (Na), and depleted in carbon (C) and oxygen (O) (e.g., Milone et al., 2013). 1G stars, in particular, reflect the chemical composition of the pristine material from which GCs formed providing the unique opportunity to study the chemistry of primordial clouds where stars formed at high redshift.

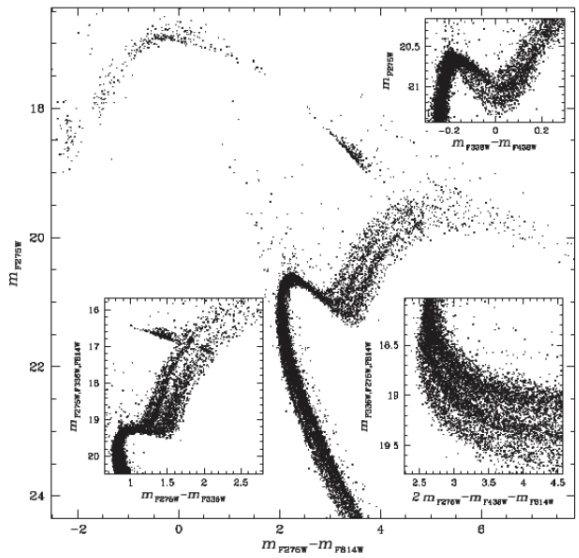

Figure 1.2: m_{F275W} vs. $m_{F275W} - m_{F814W}$ CMD for NGC 2808. Multiple sequences corresponding to MPs are clearly recognizable at all evolutionary stages. The three small panels show sections of the CMD in which different filter combinations are used to highlight the separation between MPs at distinct evolutionary stages. Figure from Milone et al. (2015b).

A powerful tool to infer the relative chemical compositions of 1G and 2G stars is the 'Chromosome Map' (ChM; Milone et al., 2015b, 2017), a pseudo two-color diagram, build with appropriate photometric bands of HST (generally F275W, F336W, F438W and F814W), which is sensitive to the chemical composition of GC stars thus allowing to maximize the separation among distinct stellar populations. This is particularly evident in the ChM shown in the left panel of Figure 1.4 where 1G and 2G stars clearly form two separate groups (respectively enclosed in the red and blue ellipses) that are not consistent with the expected distribution for a simple population of stars with the same chemical composition (orange points).

1.2 Properties of Multiple Populations

The techniques for photometric data reduction and the innovative color combinations described in Section 1.1 allowed to characterize MPs in more than 70 galactic and extragalactic GCs. The main observational features of MPs, retrieved both from photometry and spectroscopy, are the following:

- **1G-2G discreteness.** 1G and 2G stars form distinct sequences that can be traced in photometric diagrams with opportune color combinations. This separation is particularly evident in ChMs where clusters show strong evidences of MPs (Milone et al., 2017).
- **Ubiquity.** As anticipated in the previous point, using diagrams with the appropriate color combinations and ChMs, 1G and 2G stars have been found

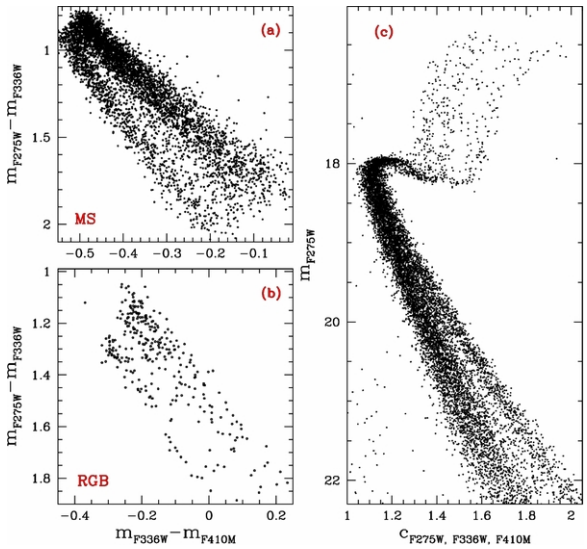

Figure 1.3: Collection of photometric diagrams that exploit combinations of UVIS/WFC3 filters for NGC 6752. *Panel (a) and (b).* $m_{F336W} - m_{F410M}$ vs. $m_{F275W} - m_{F336M}$ two-color diagrams respectively for MS and RGB stars. This kind of diagrams allows to identify distinct stellar populations only if different evolutionary stages are considered separately. *Panel (c).* m_{F275W} vs. $C_{F275W,F336W,F410M}$ diagram. Here distinct stellar sequences can be traced at all magnitudes of the pseudo-CMD. Figure from Milone et al. (2013).

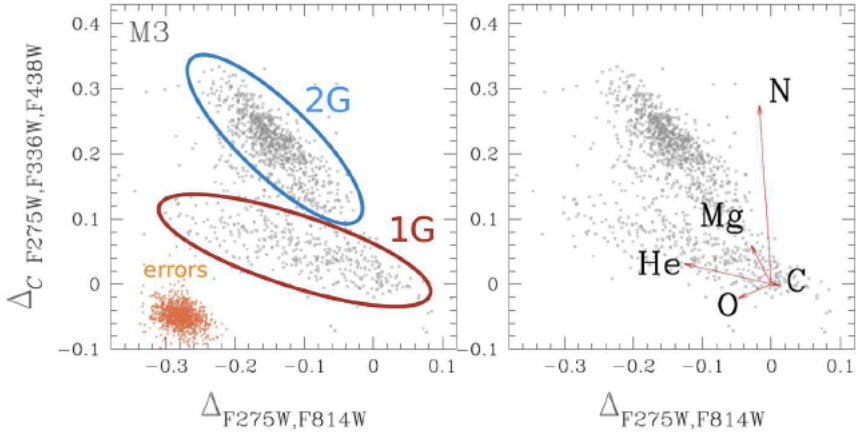

Figure 1.4: *Left.* ChM of RGB stars of M 3 (gray points) from Milone et al. (2017). The red ellipse marks 1G stars, whereas 2G stars are enclosed in the blue one. The orange points indicate the distribution expected for a simple population of stars with the same chemical composition. *Right.* The arrows indicate the effect of changing He, C, N, Mg and O, one at a time, on $\Delta_{F275W,F814W}$ and $\Delta_{C\ F275W,F336W,F438W}$. Figure from Milone (2019).

in all studied GCs (Milone et al., 2017) thus demonstrating that the formation of MPs within GCs is a common event in the Galaxy.

- **Variety.** While MPs are now considered a common feature of nearly all galactic GCs, some of their properties significantly change considering different clusters. An example is the fraction of 2G stars that ranges from $\sim 35\%$ (M 71) to more than 90% (ω Cen).

- **Two classes of GCs.** ChMs revealed that the majority of galactic GCs present single sequences of 1G and 2G stars (Type I GCs). On the contrary, a smaller fraction ($\sim 17\%$) of GCs exhibits multiple sequences of 1G and 2G stars in their ChMs (Type II GCs). Star-to-star variations in abundance of heavy elements like iron (Fe) and s-process elements seem to be responsible for the spread observed in Type II GCs, also called 'anomalous' for this reason (Yong et al., 2008; Marino et al., 2019a).

- **Helium enrichment.** One of the major challenge for modern spectroscopy is the determination of He abundance from spectral lines. As described in Section 1.1, photometric diagrams with a wide color baseline are sensitive to He variations among stars in GCs. Comparing colors observed in these diagrams with the one retrieved from synthetic spectra represents an efficient tool to overcome the limitation of spectroscopy concerning He (Milone et al., 2012a). Exploiting this technique, estimates of the internal He variation were derived for almost all known Galactic GCs. In particular, the maximum He variation is an intrinsic feature of each GC which ranges from $\Delta Y_{max} < 0.01$ to $\Delta Y_{max} \sim 0.18$ (Milone et al., 2018; Zennaro et al., 2019).

- **Dependence on GC orbit.** Clusters with $R_{PER} > 3.5$ kpc host a larger fraction of 1G stars than the ones with a small perigalactic radius (Zennaro et al., 2019) thus suggesting that interactions with the Milky Way (MW) during the entire life of the GC could have a role in 1G/2G fractions.

- **No dependence on stellar mass.** Stars with different masses within a cluster share similar properties related to the phenomenon of MP (Milone et al., 2014a, 2019). In particular, the relative amounts of 1G and 2G stars are constant in the $\sim 0.15 - 0.80$ $M_{\odot}$ mass range.

- **Anisotropic motions of 2G stars.** In massive GCs, like ω Cen or 47 Tuc, 2G stars exhibit more radially-anisotropic velocity distributions than 1G stars (Bellini et al., 2018; Richer et al., 2013). Less massive GCs, as for example M 4 or M 71, show instead isotropic velocity distributions among both 1G and 2G stars suggesting that dynamical processes could have cancelled out differences in the kinematic properties of MPs at formation (Cordoni et al., 2019).

- **More centrally-concentrated 2G.** In some GCs, such as ω Cen, 47 Tuc, NGC 2808 and M 3, 2G stars are more centrally-concentrated than 1G ones (Sollima et al., 2007; Bellini et al., 2009; Milone et al., 2012a; Cordero et al., 2013; Lee, 2019). Others GCs (NGC 6362, NGC 6752, M 5), instead, have similar radial distributions (Nardiello et al., 2015; Dalessandro et al., 2018; Milone et al., 2019).

- **GC Specificity.** 2G stars, although common to all GCs, are instead very rare in the MW field thus suggesting that their formation could be a distinctive feature of GCs.
- **Supernova (SN) avoidance.** Excluding some Type II GCs, no variations in metallicity between 1G and 2G stars were detected thus indicating that GCs have retained a small fraction of SN products that did not appreciably contaminate 2G stars.
- **Hot CNO and NeNa processing.** 2G stars, being enhanced in He, N, Na and depleted in C and O (as anticipated in Section 1.1), exhibit the chemical composition resulting from CNO cycling and p-capture processes at high temperatures.
- **Dependence on cluster mass.** The fraction of 1G stars strongly anti-correlates with both the present-day and the initial GC mass. The maximum internal variations of He and N, instead, correlate with the host cluster mass (Milone et al., 2017, 2018). Consequently, the incidence and the complexity of MPs increase with cluster mass.
- **Mass-budget problem.** As already pointed out, in most GCs 2G stars are the dominant component, especially in central regions where their fractions can largely exceed $\sim 50\%$. The predominance of the 2G component raises a major challenge for every formation scenario because only a small fraction of the initial 1G mass is delivered with the composition required to form 2G stars. A possible solution for this problem consists in postulating that GC progenitors were substantially more massive and that have lost at least $\sim 80 - 90\%$ of their mass before delivering the naked present-day GCs.

1.3 Formation Scenarios of Multiple Populations

To interpret the observational properties of MPs it has been initially suggested that GCs have experienced multiple bursts of star formation, with 1G stars formed initially from the pristine proto-GC material, and one or more subsequent events where 2G stars form from material polluted by the ejecta of massive 1G stars. As anticipated, 2G stars are typically enriched in He, N and Na and depleted in C and O thus exhibiting the chemical composition resulting from CNO cycling and p-capture processes at high temperatures. Therefore, possible 1G sources of the processed material include all kinds of stars in which those elements are produced at such temperatures and then ejected in the intra-cluster medium.
The nature of the 1G polluters is still debated. Examples of the proposed candidates are:

- **Supermassive Stars (SMSs).** Denissenkov and Hartwick (2014) and Denissenkov et al. (2015) proposed the idea that within a young GC the most massive stars fall towards the center as a result of dynamical friction. Once reached the center, massive stars undergo multiple collisions with each other leading to the formation of a SMS, an object with a mass that should be in a very precise range around $\sim 10^4$ $M_\odot$. Stars with similar masses are fully convective, hence chemically homogeneous, and characterized by luminosities close to the Eddington limit, allowing for a consistent mass loss. As the SMSs

evolve, their winds would be progressively enriched in He and products of CNO cycling and p-processes reactions, exactly the composition demanded to reproduce observations of 2G stars.
The GC environment is instrumental for the formation of the central SMS thus the GC specificity requirement is fulfilled. Beyond this, also the variety and discreteness of MPs may be accomodated appealing respectively to different masses of the SMS and separate bursts of star formation. Nevertheless, this model fails to reproduce some observational requirements, as for example SN avoidance, mass budget and helium enrichment.

- **Fast Rotating Massive Stars (FRMSs).** According to the current version of this model (Krause et al., 2013), the polluters are massive stars ($\sim 25-150$ $M_\odot$) characterized by fast rotation that allows the transport of hydrogen (H) burning products from the convective core to the radiative envelope. FRMSs continuously loose mass through a slow mechanical equatorial wind forming a decretion disk around them, eventually fed also by pristine gas coming from the surroundings. 2G stars may then originate in these disks after the development of gravitational instabilities within them.
This model has difficulties in reproducing some of the observational constraints, for instance GC specificity. Indeed, if this process occurs in nature, there are no reasons to not have these stars also in other regions of the Galaxy. Therefore, the result would be that 2G stars would be found not only in GCs but also in the Galactic halo field, which is however in contrast with observations. Another insurmountable issue is related to the discreteness of the 2G component since the distribution of chemical abundances are expected to be continuous. Furthermore, also SN avoidance, mass budget and detailed chemical composition of 2G stars are major problems for this scenario.

- **Asymptotic Giant Branch (AGB) stars.** Hot Bottom Burning (HBB) is a peculiar nucleosynthesis process during which very high temperatures are reached at the bottom of the convective envelope thus allowing efficient p-capture nuclear processing (Ventura et al., 2013). HBB characterizes the AGB phase of stars with masses from $\sim 3-4$ $M_\odot$ to ~ 8 $M_\odot$. This mass range, however, should be regarded as indicative since the maximum temperature reached at the base of the envelope strongly depends on the model assumed to describe the convection. Hence, the mass range may be extended to include also the so called super-AGB stars, characterized by masses up to ~ 10 $M_\odot$. On the other hand, the lower limit must be fixed at ~ 3 $M_\odot$, otherwise the HBB process would not operate and the AGB would be populated by carbon stars. Such objects, however, are not observed among 2G allowing to conclude that the formation of 2G stars must be completed before ≤ 3 $M_\odot$ stars reach the AGB phase.
According to the version of this model proposed by D'Ercole et al. (2010), the GC progenitor has a major episode of star formation that leads to the 1G population. Then, massive 1G stars explode as SNe clearing any remaining gas from within the cluster. After > 30 Myr, AGB (and Super-AGB) stars start ejecting material that tends to accumulate in the cluster since its ejection velocity ($\sim 10-30$ km/s) is lower than the escape velocity. This material cools and falls towards the center and, once a critical density is reached, one or more starburst episodes occur leading to the formation of 2G stars. In

the subsequent dynamical evolution of the system, tidal interactions with the parent galaxy strip away a large fraction of 1G stars into the Galactic field leaving the present-day structure.
This model is able to reproduce most of the observational properties of MPs. A major problem is related to the fact that AGB stars tend to produce a correlation between O and Na, in contrast with the observed anticorrelation. To solve this issue, the model requires that AGB yields accrete large amounts of pristine material from the surroundings before 2G stars form.

The alternative scenario suggests instead that there is only one star formation episode and then some of the 1G stars accrete material ejected from the more massive stars of the same generation. In this context, three main models can be mentioned:

- **Massive Interacting Binaries (MIBs).** De Mink et al. (2009) modelled a binary interaction between two stars, respectively with mass of 20 and 15 $M_{\odot}$, to investigate the yields of the ejected material. In MIBs the forced rotation of the primary stellar envelope would cause internal mixing that brings H-burning products from the core to the envelope of the star. The processed material would then be spread outside in a subsequent common-envelope phase of the MIB, polluting the interstellar medium (ISM). In the original version proposed by De Mink et al. (2009), 2G stars form out of this material whose composition matched the observed trends in GCs (i.e. He enhancement, O depletion, etc.).
  This model is certainly GC-specific and might also fulfill the requirement linked to variety. Nevertheless, it encounters insurmountable difficulties in reproducing the discreteness of MPs. Large and continuous chemical differences are indeed expected in the swept/accreted material thus preventing the formation of discrete chemical compositions observed for 2G stars in all GCs. Another major problem encountered by this model is related to SN avoidance. Indeed, like all the scenarios that operate in the first few Myr of a cluster's life, after $3-8$ Myr core collapse SNe begin to explode so that the ISM could not be made exclusively of the MIB common-envelope ejecta.

- **Early Disk Accretion.** Bastian et al. (2013) suggest an alternative version of the model described in the previous point. Specifically, the enriched material ejected from MIBs, as well as from FRMSs, pollute low mass stars that formed in the same epoch of their high mass counterparts. MIB and FRMS ejecta would be swept up by the protoplanetary disks of stars with $M < 2$ $M_{\odot}$ and eventually accreted onto the host star themselves.
  Approximately, this model is affected by the same problems discussed before for MIBs. Beyond them, another important issue is related to the fact that, in order to mix the accreted material throughout the star, the latter must be fully convective. This means that the accretion timescales would be very short ($1-3$ Myr; Salaris and Cassisi, 2014; D'Antona et al., 2015) thus strictly limiting the amount of processed material that can be accreted.

- **Super Massive Stars.** According to the model of Gieles et al. (2018), the processed material comes from SMSs ($> 10^3$ $M_{\odot}$). Because of continuous gas accretion, the proto-cluster undergoes adiabatic contraction leading to the increase of stellar density that in turns causes stellar collisions at high rate.

Therefore, if the cluster reaches sufficiently high density, a runaway collision process can form a SMS that will loose material enriched by HBB products into the intra-cluster environment where it mixes with pristine gas. This diluted material is then accreted by the proto-stars forming further stellar generations until the SMS burns out or explodes. Because the latter could be continuously rejuvenated by stellar collisions, the amount of material ejected by the SMS can be 10 times higher than its mass thus providing a feasible solution for the mass-budget problem.
One major advantage of this model is that it predicts a super-linear scaling between the amount of processed material and cluster mass, which indeed is in agreement with observations. On the contrary, one of the major drawbacks is that SMSs are still only theoretical, even if there are some promising observational evidences of stars with M $>$ 100 $M_{\odot}$ (e.g., Crowther et al., 2016).

Despite GCs have always been among the most studied stellar systems, astronomers still have to understand how they formed in the early Universe. After the discovery of MPs, that is a well-established fact nowadays, achieving this task became even harder than ever before and currently none of the previously described scenarios succeed in giving a completely satisfying explanation about the origin of GCs. All of them, indeed, encounter serious difficulties in fulfilling one or more observational constraints that can not be ignored.

1.4 An unexpected discovery: the extended first-generation

Recent work has identified 1G and 2G stars in 57 Galactic GCs based on the ChMs of their RGB stars (Milone et al., 2017) that, as anticipated in Section 1.1, constitute one of the most powerful tool to isolate and identify MPs. These sort of two-color diagrams, normally obtained by combining F275W, F336W, F438W and F814W filters of HST, are particularly sensitive to the chemical composition of stars. Indeed, their y-axis, being sensitive to the spectral energy distribution (SED) in the UV and optical blue, depends on the abundance of C, N and O. In reality, as show in the right panel of Figure 1.4, only the N abundance is able to affect considerably $\Delta_{\mathrm{C\,F275W,F336W,F438W}}$. The x-axis, instead, is connected to the shape of SED in the UV and in the NIR thus being approximately a measure of effective temperature. Both He and Fe variations can, in principle, modify the effective temperature of stars in GCs thus causing a variation in $\Delta_{\mathrm{F275W,F814W}}$. Indeed, stars with a higher He mass fraction, having lower opacity, reveal to be hotter while metal-rich stars are cooler with respect to metal-poor analogues.
In ChMs of nearly all observed GCs the distribution of 1G and 2G stars is wider than that expected from observational errors alone thus demonstrating that both 1G and 2G stars are not chemically homogeneous. This phenomenon can be naturally explained for 2G stars using the dependence of $\Delta_{\mathrm{F275W,F814W}}$ and $\Delta_{\mathrm{C\,F275W,F336W,F438W}}$ on light elements abundances. As illustrated in the right panel of Figure 1.4, the 2G spread can be easily reproduced by a combination of N and He vectors that is expected for 2G stars characterized by a chemical composition produced by various degrees of CNO processing. The extension of the 1G sequence, instead, has revealed to be a more puzzling result since, in principle, these stars should all have the same

chemical composition within each GC. Several hypothesis were suggested to explain this intriguing feature observed in ChMs of many Type I GCs.
Milone et al. (2015b, 2018) attributed the 1G spread to a pure He variation among 1G stars without any appreciable enrichment in other light elements abundances, like N. This can be easily understood from the right panel of Figure 1.4 where He vector is almost perfectly superimposed to the 1G extension that spans a quite large range in $\Delta_{\rm F275W,F814W}$ while approximately sharing the same $\Delta_{\rm C\,F275W,F336W,F438W}$, hence the same N abundance. Such a trend, however, can not be explained through the hot H-burning associated to CNO cycle that has generally been adopted to explain the observed chemical patterns in GCs. The extended 1G seems, instead, to be more linked to p-p chain H-burning, as described in details in Section 8 of Milone et al. (2018). Here, some scenarios that could explain a pure He variation are discussed but none appears to work. In addition, Tailo et al. (2019) found that variations in He abundance among 1G stars lead to inconsistent results regarding the HB stellar distribution, the period distribution of RR Lyrae variable stars, and the color distribution of the MS stars. For these reasons, He variations, while in principle could be able to reproduce the 1G extension observed in many ChMs, seem unlikely.
An alternative hypothesis was suggested by Marino et al. (2019a). Combining space and ground-based photometry with spectroscopical measurements available for some stars in different GCs, they found that similar spreads in He or Fe among 1G stars could be responsible for the extended 1G sequence. Since, as pointed out previously, a small spread in He without variations in other light elements is extremely difficult to explain in terms of nuchleosynthesis, a similar spread in metallicity seems to be much more plausible. Indeed, Fe inhomogeneities of the order of ~ 0.1 dex in the cloud generating 1G stars could be originated by incomplete mixing of the SN ejecta thus suggesting that SNe had an important role in the star formation history of most GCs. In light of these results, Marino et al. (2019b) extended high-resolution spectroscopical measurements to 18 1G stars in NGC 3201 finding a small variation in metallicity (~ 0.1 dex) among them. Three of the 18 stars revealed to be binary candidates allowing to conclude that also binarity could contribute to the elongation of the 1G stars producing a shift especially towards lower $\Delta_{\rm F275W,F814W}$. Nevertheless, as pointed out also by Martins et al. (2020), unless binary fractions in GCs are actually severely underestimated, binaries alone can not fully explain the extended 1G sequence since only binaries with $q > 0.8$ are able to produce an appreciable shift of $\Delta_{\rm F275W,F814W}$ towards lower value (Marino et al., 2019b).
Concluding, since the 1G color spread has been observed mostly in ChMs of evolved RGB stars, also stellar evolution, in principle, could be responsible for this intriguing phenomenon producing star-to-star chemical variations among the 1G component.

1.5 Thesis layout

The color spread of 1G stars observed in many ChMs constitutes by far one of the major challenges in the understanding of MPs for which astronomers have not found a solution yet. At the same time, as already pointed out in Section 1.1, investigating the origin of the elongated 1G sequences may also provide the unique opportunity to trace the chemical composition of primordial clouds where 1G stars formed.

With the aim of shedding new light on this intriguing phenomenon, in this thesis I combine multi-band HST photometry and synthetic spectra analysis techniques to investigate for the first time chemical variations among unevolved MS stars of the galactic GC NGC 6362. This cluster presents a well-elongated 1G population on the ChM of its RGB stars (see Figure 4 of Milone et al., 2017) thus constituting an ideal target for studying in more details this phenomenon. Starting from the results obtained for NGC 6362, I extend then my considerations to 55 Galactic GCs searching for correlations with the main host GC parameters.

The thesis is organized as follows: Chapter 2 describes the photometric dataset for NGC 6362 and the procedures employed to reduce it. Chapter 3 illustrates how the images were analyzed combining them with the synthetic spectra techniques. Finally, results are presented in Chapter 4 that contains also a brief summary of the entire work.

Chapter 2

Observations and data reduction

In this Chapter, I present the analyzed dataset for the Galactic GC NGC 6362 together with the techniques employed for data reduction. In particular, Section 2.1 describes briefly the instrumentation on board HST used to collect the set of images exploited in this thesis. Then, Section 2.2 presents in more details the dataset available for NGC 6362 whose reduction is explained respectively in Section 2.3, 2.4 and 2.5.

2.1 Instrumentation

High-precision photometry provided by HST has been instrumental for the characterization of MPs in GCs. Orbiting around the Earth since 1990, HST is not affected by distortions introduced by the atmosphere allowing to obtain diffraction limited images. HST has also another advantage, namely the possibility to observe at wavelengths that are inaccessible to ground-based telescopes. This is extremely important for the study of MPs in GCs since, for example, observations in the UV spectral region are crucial to identify stars with different He and light elements abundances.
HST currently hosts 6 different instruments on board:

- **Advanced Camera for Surveys (ACS).** ACS includes three independent channels:
  - High Resolution Channel (HRC);
  - Solar Blind Camera (SBC);
  - Wide Field Camera (WFC), covering a wavelength range of $\sim 3500 - 11000$ Å.
- **Wide Field Camera 3 (WFC3).** WFC3 includes two independent channels:
  - UVIS, observing at a wavelength range of $\sim 2000 - 10000$ Å, including UV spectral region;

DATE	N × EXPTIME	INSTRUMENT	FILTER	PROGRAM	PI
2014 March 30	$2 \times 720\,s$	UVIS/WFC3	F275W	13297	G. Piotto
2014 July 01	$2 \times 829\,s$	UVIS/WFC3	F275W	13297	G. Piotto
2010 August 13	$368\,s + 4 \times 450\,s$	UVIS/WFC3	F336W	12008	A. Kong
2014 March 29	$323\,s$	UVIS/WFC3	F336W	13297	G. Piotto
2014 March 30	$323\,s$	UVIS/WFC3	F336W	13297	G. Piotto
2014 July 01	$2 \times 323\,s$	UVIS/WFC3	F336W	13297	G. Piotto
2014 March 29	$68\,s$	UVIS/WFC3	F438W	13297	G. Piotto
2014 July 01	$67\,s$	UVIS/WFC3	F438W	13297	G. Piotto
2006 May 30	$10\,s + 4 \times 130\,s$	WFC/ACS	F606W	10775	A. Sarajedini
2011 March 30	$140\,s + 145\,s$	WFC/ACS	F625W	12008	A. Kong
2011 March 30	$750\,s + 766\,s$	WFC/ACS	F658N	12008	A. Kong
2006 May 30	$10\,s + 4 \times 150\,s$	WFC/ACS	F814W	10775	A. Sarajedini

Table 2.1: Summary of the information about archive images of NGC 6362 used in this work.

  - IR.

- **Cosmic Origins Spectrograph (COS).**
- **Near Infrared Camera and Multi Object Spectrometer (NICMOS).**
- **Space Telescope Imaging Spectrograph (STIS).**
- **Fine Guidance Sensors (FGS).**

2.2 Dataset

In this work, the astro-photometric catalog of the galactic GC NGC 6362 was obtained starting from the archive images available respectively for three filters (F275W, F336W and F438W) of the UVIS/WFC3 and four filters (F606W, F625W, F658N and F814W) of the WFC/ACS on board HST. The main properties of these exposures are summarized in Table 2.1.

2.3 The Effective Point Spread Function

In HST images of GCs the majority of objects are relatively isolated point-source stars that can be described using the coordinates (x, y) of center position and the total flux (f). These three parameters are obtained by fitting the PSF to the array of pixels which constitutes the image. The critical points of this procedure are exemplified in Figure 2.1. First of all, it can be seen that the stellar profile represented by the histogram is matched by both the models of PSF. Despite fitting well the stellar profile, the latter yield different estimates for the star center position, separated by a distance (0.07) that is not consistent with random errors alone (0.02). This is the so-called pixel-phase error which arises from the fact that the PSF formed by HST has a core of 50 mas poorly sampled by the WFC/ACS pixel size (100 mas). Furthermore, another related issue is the fact that it is difficult to choose which of the 2 PSFs better fits the stellar profile. The only way to achieve this task implies to know with great accuracy the position of the star but there is no chance to get it without accurately knowing the PSF. This degeneracy can be broken using the

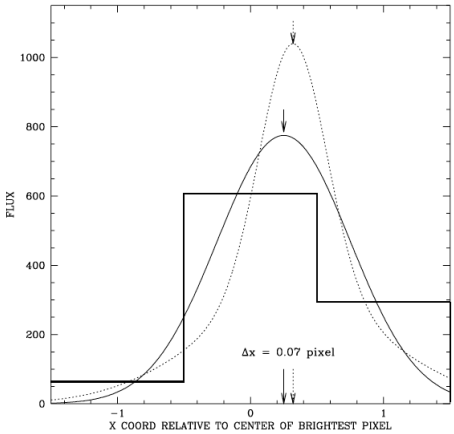

Figure 2.1: One-dimensional stellar profile fitted by two different models of PSF whose peaks do not coincide. This fact leads to a different estimate of the star center. Figure from Anderson and King (2000).

dithering technique which consists of taking multiple images slightly shifted in order to have the star centroid at different locations with respect to pixel boundaries.
These considerations clearly demonstrate the need for an accurate PSF. To achieve this task, Anderson and King (2000) developed an innovative approach based on the so-called effective PSF (ePSF). In practice, if in the vicinity of a pixel $(i,\ j)$ there is a point source whose center is $(x_*,\ y_*)$, the flux in that pixel will be:

$$P_{ij} = f_* \int_{-\infty}^{\infty} \mathscr{R}(x-i, i-j)\psi_I(x-x_*, y-y_*)\, dxdy + s_* \tag{2.1}$$

where f_* is the stellar flux, $\mathscr{R}$ is the sensitivity profile of a pixel, $\psi_I(\Delta x, \Delta y)$ is the instrumental PSF (iPSF) and s_* is the value of the background at that pixel.
After some algebraic calculations it can be shown that this pixel value is the result of a convolution between the iPSF and the sensitivity profile of a pixel:

$$P_{ij} = f_* \int_{-\infty}^{\infty} \mathscr{R}(-x, -y)\psi_I(\Delta x - x, \Delta y - y)\, dxdy + s_* \tag{2.2}$$

which is equivalent to:

$$P_{ij} = f_*\psi_E(i-x_*, j-y_*) + s_* \tag{2.3}$$

where:

$$\psi_E(\Delta x, \Delta y) = \int_{-\infty}^{\infty} \mathscr{R}(-x, -y)\psi_I(\Delta x - x, \Delta y - y)\, dxdy \tag{2.4}$$

is the ePSF, a continuous function smoother than iPSF.
The ePSF has three major advantages with respect to iPSF:

- **Simplicity.** The fitting of the PSF to a stellar image requires no integration since it consists only in finding the values of x_*, y_* and f_* that minimize the sum of the squares of the residuals.

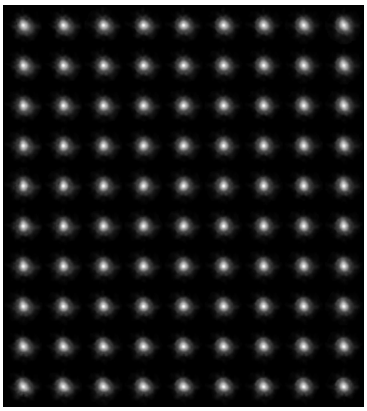

Figure 2.2: An example of the 9×10 grid of ePSFs for one of the exposures taken by WFC/ACS in F606W filter.

- **Easier to solve for an ePSF than for an iPSF**. Turning equation (2.3) around the ePSF can be estimated by:

$$\hat{\psi}_E(\Delta x, \Delta y) = \frac{P_{ij} - s_*}{f_*} \tag{2.5}$$

  So knowing x_*, y_* and f_*, an estimate of ePSF for each pixel can be easily derived. On the other hand, the conventional practice of trying to deduce the iPSF from observed pixel values requires basically a deconvolution that is by far much more complicate.

- **Better accuracy.** Since using the ePSF bypasses the problem to disentangle between the contributions of iPSF and $\mathscr{R}$, any assumptions about how sensitivity varies within a pixel can be avoided.

2.3.1 Deriving the ePSF for NGC 6362

In order to obtain the best possible PSF, fundamental to have the best possible photometry and astrometry, the techniques presented in Section 2.3 were applied for each exposure of NGC 6362 using the fortran routine `img2psf` (Anderson and King, 2000), specifically adapted to reduce images taken with UVIS/WFC3 and WFC/ACS. One of the most innovative features of these programs is the iterative procedure, crucial to retrieve an accurate model for the PSF. Indeed, a PSF cannot be derived from an image without knowing a priori the star positions and fluxes but at the same time the latter can not be measured without recourse to a PSF. In practice, the routines that I used in this work alternated between deriving the PSF and measuring the stars improving both at each iteration, consisting basically on three stages:

1. All pixel values P_{ij} in the image are converted to an estimate of one of the points that form the ePSF using the equation (2.5) with the most recent values of x_*, y_* and f_*.

2. The ePSF obtained in the previous stage is used to retrieve a new estimate of x_*, y_* and f_* for each star by least squares fitting.

3. The multiple observations are brought to a common reference system in order to average together the most recent estimates of x_*, y_* and f_* allowing to obtain much accurate positions and fluxes than individual measurements. Finally, these new measurements are transformed back into the frame of each individual image.

The iterative process is applied only for isolated, bright but not-saturated stars of each exposure and needs, at the beginning, a pre-computed library PSF as a starting guess to derive the raw star positions and fluxes. The criteria required by the routines to derive the best possible PSF are specified in their 7 arguments:

- **HMIN.** It is used to select isolated stars. In particular, it defines the minimum separation (in pixels) between two sources in order to be considered. A typical value could be 11.
- **FMIN.** It is used to select the minimum value of flux (expressed in counts) that a source can have to be considered. A typical value could be 3000.
- **PMAX.** It is used to select the maximum value of flux (expressed in counts) that a source can have to be considered. Since saturated stars have to be excluded, a typical value here is 54999, immediately below the saturation limit.
- **QMAX.** It is used to define the maximum value of the Q parameter that describes the quality of the fit. A typical value aimed to exclude nearly all non-stellar sources is 0.2.
- **NSIDEs.** It is used to define the grid sampling for the PSF and ranges from 1 to 5. In particular, taking into account a large number of different regions helps to contrast the problem of the PSF spatial variations but at the same time decreases the number of stars used to calculate the PSF. A compromise is reached using a value of NSIDEs equal to 3.
- **PSFFILE.** It is used to select the initial library PSF to be used.
- **IMG.fits.** It is used to define the sequence of images to be analyzed.

As represented in Figure 2.2, the programs do not compute a single PSF but a grid of 9×10 PSFs. This is necessary to account for the fact that, because of position-dependent charge diffusion and optical aberrations, the PSF could change its shape with location on the detector. A PSF model is then obtained for any point interpolating the PSF among the four nearest grid points.
After deriving the PSF, another fortran routine, `img2xym` (Anderson and King, 2006), was used in order to obtain positions and instrumental magnitudes of stars by fitting the just derived PSF model to each exposure. This time, since the PSF has to be applied to all the sources of the image, from faint to saturated stars, the parameters used are less restrictive than before: HMIN = 3, FMIN = 50, PMAX = 99999. The program also offers the possibility to check the quality of the PSF fitting procedure with the *SUBT* flag that creates a star-subtracted image. The main final output is a file with `.xym` extension which has one line for each source

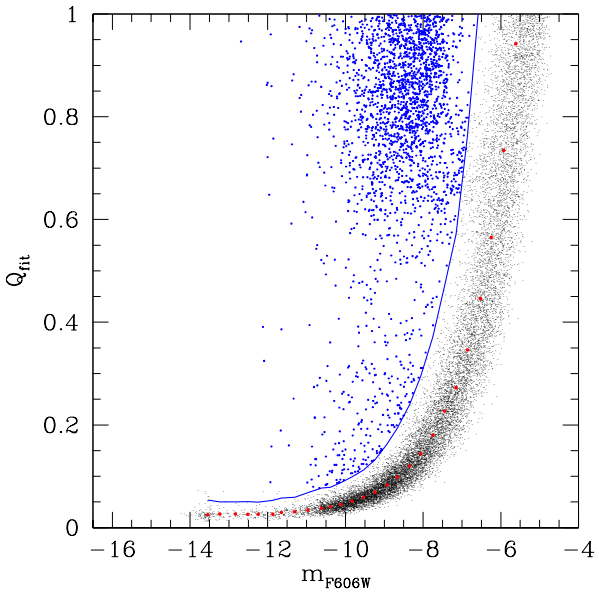

Figure 2.3: 'Cleaning' process for one exposure in F606W filter taken as example. Blue dots represent the discarded sources while black ones correspond to accepted stars. Red dots correspond instead to the median value of Q_{fit} for every magnitude bin. The blue line, finally, represents the fiducial corresponding to median points plus 3σ.

found, giving the coordinates (x, y), the instrumental magnitude ($-2.5\log(\text{flux})$) and the Q parameter, fundamental to discriminate between real stars and other sources in the following.

2.4 Catalog Building

This Section explains how the astro-photometric catalog for stars in NGC 6362 was built. Specifically, the images were reduced using two different methods:

- **First-Pass Photometry (Section 2.4.1).** Every image is reduced singularly and then exposures in each filter are put together. This method is particularly suitable to improve the precision of measurements for bright stars.

- **Second-Pass Photometry (Section 2.4.2).** All the exposures in each filter are stacked in a single image from which positions and magnitudes are then obtained. This method gives better results for faint stars.

In order to retrieve the best possible photometry for NGC 6362, the results obtained using the two methods are then combined in a single final catalog containing the most accurate measurements for both faint and bright stars.

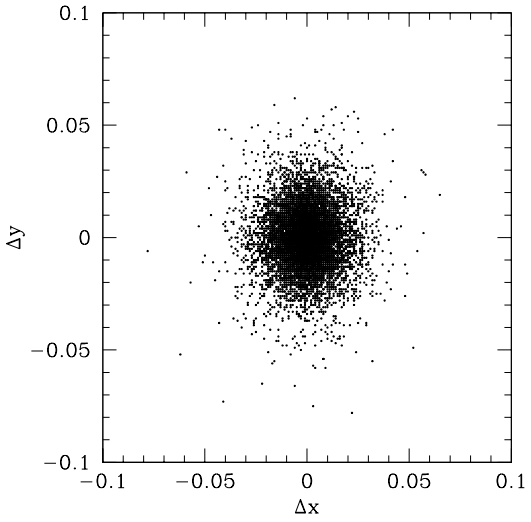

Figure 2.4: Example of transformation residuals between one of the exposure in the F814W filter and the master frame.

2.4.1 First-Pass Photometry

The last program presented in Section 2.3.1 processes all sources that satisfy the criteria imposed as if they were stars but some of these have to be removed since they could be cosmic rays, hot pixels, PSF artifacts or noise spikes. To accomplish this task, I used a SuperMongo routine which plot the Q parameter as a function of the instrumental magnitude rejecting sources that are above the blue fiducial line in Figure 2.3. It is important to stress that this kind of 'cleaning' process was only applied for objects with $mag > -13.7$ thus keeping all saturated stars that will be necessary for next steps of data reduction. The final output of this program is a catalog for every image containing positions and magnitude for all the identified stars.
Coming from different exposures, these catalogs are not perfectly matched. Therefore, the next step is to combine them to obtain a single catalog for each filter. To accomplish this task, first of all, I choose an image for each filter to be used as reference frame (master frame). Then, I used `xym2mat`, `xym2bar` and `xym1mat`, a set of fortran routines developed by Jay Anderson that finds the correct coordinate transformation to bring each image in the same reference system of the master frame. Specifically, `xym2mat` finds the same stars in different catalogs through two different iterations. In the first one, only the brightest stars, including saturated ones, are identified. Then, the program uses a method called *Cross Identification* consisting in looking for similar triangles of stars between the master frame and the analyzed exposure. In this way, it can identify common objects in different catalogs whose coordinates, both in the master and in the image reference frame, are used to calculate, by least squares fitting, the 6 coefficients of the transformation that allows to bring all the images in the same reference frame (the master one):

$$\begin{cases} x_1 = A + C \cdot x_2 + E \cdot y_2 \\ y_1 = B + D \cdot x_2 + F \cdot y_2 \end{cases} \tag{2.6}$$

where (x_1, y_1) and (x_2, y_2) are the coordinates of the same star respectively in the master and the considered image reference frame while *A, B, C, D, E* and *F* are the coefficients of the transformation. The latter are used as a starting point for the second iteration in which the same operation is repeated excluding saturated stars since they are not well measured. The final output is a series of MAT.xxx files containing positions (both in the master and in the image reference frame) and instrumental magnitudes of common stars together with residuals of the transformations. Figure 2.4 represents an example of the residuals for one of the image in the F814W filter: it has a nearly circular distribution centered at 0, thus suggesting that the program found plausible transformations. The MAT.xxx files are used by the second fortran routine `xym2bar` to compute average positions and instrumental magnitudes of common stars with $mag < -5.5$. As anticipated, fainter stars are excluded since they will be analyzed properly using different techniques presented in Section 2.4.2. The program requires only one argument that is the minimum number of images in which the same star has to be individuated to be considered. The final output is a single catalog for each filter where every row corresponds to a measured star for which the average position and instrumental magnitude are listed. Finally, the third fortran routine `xym1mat` links two catalogs in different filters, after choosing one as reference (in the case of NGC 6362 I selected the F814W catalog as master), finding common stars between them. To speed up the process, first I considered only bright stars and then I allowed the program to link all the stars.
At this point, after using the set of fortran routines previously described, I obtained one catalog for each filter linked to the F814W one. Since every catalog has its own reference frame, the one of the image selected as master, the next step was to express stars coordinates in an absolute reference frame, that is the one provided by GAIA. To achieve this task, first I downloaded the catalog of NGC 6362 from the GAIA Data Release 2 (Gaia Collaboration et al., 2016, 2018)[1] and then I transformed in linear coordinates (*x, y*) the stars positions expressed in right ascension (RA) and declination (DEC). After doing that, I linked the catalog in the F814W filter to the GAIA one in order to obtain a new master frame with GAIA coordinates and HST instrumental magnitudes. The latter was employed to retrieve a new F814W catalog used then as a starting point to obtain new catalogs also for the other filters. Concluding, as done previously, these new catalogs have been respectively linked to the F814W one.

2.4.2 Second-Pass Photometry

The catalogs produced in Section 2.4.1 do not contain information about the faintest stars of NGC 6362 since their S/N is very low in individual images. Second-pass photometry allows to identify and measure them by combining in a proper way the information of all the single images for each filter. To accomplish this task, I used another fortran routine, `kitchen_sync2` (`KS2`; Anderson et al., 2008a), that takes as input single images in each filter (paying attention to divide them in long and short exposures), the PSF already derived in Section 2.3.1 and the set of MAT.xxx files (Section 2.4.1) containing the transformation between each image and the master frame. The finding procedure is accomplished through different iterations, 6 for the specific case of NGC 6362. In the first one, starting from a catalog provided

[1] Downloaded from `https://gea.esac.esa.int/archive/`.

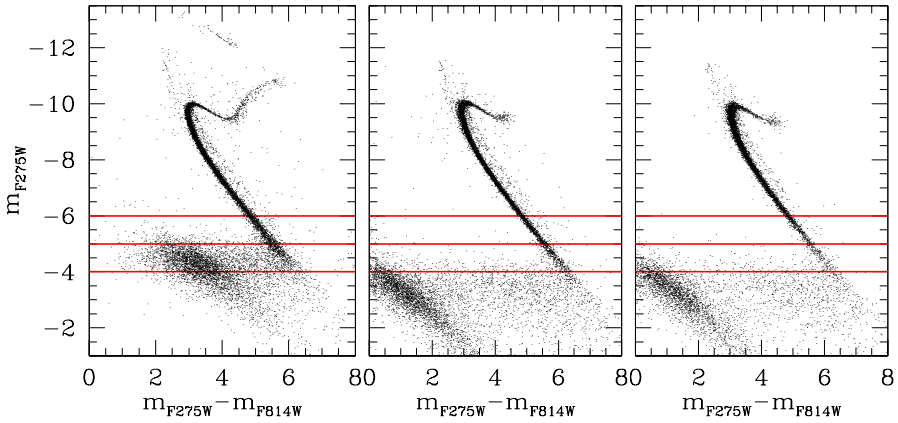

Figure 2.5: m_{F275W} vs. $m_{F275W} - m_{F814W}$ CMD obtained with the three different methods of KS2. Red horizontal lines are drawn to underline that for faint stars (instrumental $m_{F275W} > -5$) methods 2 and 3 give more accurate measurements.

by first-pass photometry, the software identifies only the bright stars whose fluxes are measured only in the short exposures. Then, after subtracting them, it looks for progressively fainter stars that satisfy a set of different criteria based on the Q parameter, on the distance or on the peak position.
The main outputs given by the program are three astro-photometric catalogs that are respectively obtained with three different methods (see Bellini et al., 2017 for more details). The first approach allows to measure well only the brightest (unsaturated) stars since it can measure positions and fluxes only when a star generates a distinct peak within its local 5×5 pixel neighbor-subtracted raster. Fainter stars often do not produce a significant peak in all the exposures and so most of them are missed by this approach making necessary to develop other solutions for finding them. To this aim, method two and three were introduced: they basically use the position determined in the finding stage together with the PSF to perform weighted aperture photometry of the star in a neighbour-subtracted raster of 3×3 pixel. These approaches are particularly suited for crowded environments with the third one that differs from the second only by the fact that it uses only pixels inside a radius r = 0.75 pixel from the center of the star. The difference between the three methods can be seen in Figure 2.5: the first approach (left panel) allows to obtain more accurate photometry for bright stars while the second and the third one (respectively middle and right panel) provide better measurements for faint stars.
Additionally, KS2 also outputs stacked images for each specified slot. In the case of NGC 6362, before launching the program I defined 9 slots, one per each filter excluding F606W and F814W for which I also separated between long and short exposures, thus obtaining the same number of stacked images. The latter are quite useful since they allow to understand if the choices made to identify and measure stars are appropriate or if they can be improved.
Finally, KS2 offers the possibility to perform artificial-star (AS) experiments that have been used to estimate the photometric uncertainties extending to NGC 6362 the procedure introduced by Anderson et al. (2008a). Briefly, the program takes as input a list of stars with given spatial coordinate and magnitude and then analyzes

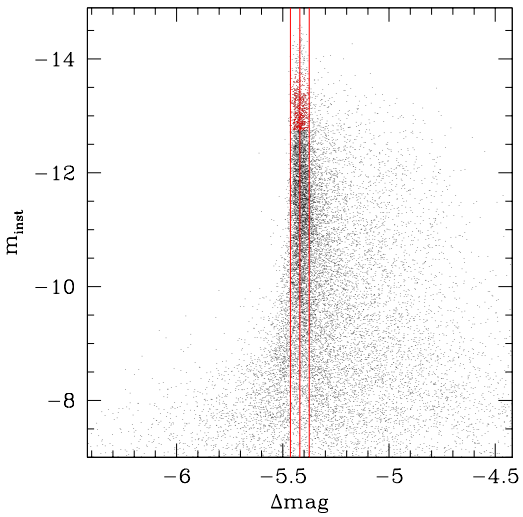

Figure 2.6: m_{inst} vs. Δmag for exposures in F814W filter. Red dots represent the bright and well measured stars used to compute Δmag while vertical lines correspond to the median Δmag (central) and the median $\pm 2\sigma$ (lateral).

them by adopting the same procedures employed for real stars. In the analysis I included only ASs with high astrometric and photometric quality that have been selected applying the same stringent criteria used for real stars.

2.5 Calibration

The last operation of data reduction is calibration that allows to give physical meaning to instrumental magnitudes used until now. To this aim, I used `drz` images that are quite different from the ones analyzed in the previous sections: they are indeed a sort of stacked images with an exposure time of 1 s, so that the values associated to each pixel is the number of counts per second. Calibrated magnitudes are retrieved using the relation:

$$m_{cal} = m_{inst} + \Delta mag + ZP_{filt} + C \tag{2.7}$$

where m_{inst} is the instrumental magnitude, Δmag is the difference between magnitudes computed using PSF photometry and magnitudes retrieved from aperture photometry, ZP_{filt}[2] is the zero-point correction for a given filter and C is the aperture correction.
To compute Δmag, I used the fortran routine `drz_phot_gfortran` developed by Jay Anderson, that basically performs aperture photometry for exposures in `drz` format. This program requires four arguments chosen in order to consider only isolated and bright (but not-saturated) stars. The routine also gives the opportunity to specify how aperture photometry will be performed specifying the aperture

[2]Retrieved specifying the filter and the observation date from `https://acszeropoints.stsci.edu` for observations with WFC/ACS and from `https://www.stsci.edu/hst/instrumentation/wfc3/data-analysis/photometric-calibration` for UVIS/WFC3.

radius and respectively the inner and outer radius of an annulus defined to measure the sky level. In principle, increasing the aperture radius allows to measure all the flux of the star. Nevertheless, it is not so simple because with a large radius also the flux of the surrounding stars is measured. To avoid this contamination, I tried to find the best compromise increasing the aperture radius as much as possible without including nearby sources flux. After measuring the aperture magnitudes for stars in each `drz` images, I used a SuperMongo routine to estimate Δmag for each filter. In practice, the routine uses only the brightest and better measured stars to calculate the median Δmag, refined at each iteration until the computed value no longer changes. Figure 2.6 shows an example of the final result of these iterations. Once Δmag was obtained, it was possible to calculate for each filter the constant that has to be added to instrumental magnitudes for transforming it in physical quantities. This operation allowed to finally obtain a high precision astro-photometric catalog for NGC 6362 concluding the part of data reduction.

Chapter 3

Data Analysis

One of the most unexpected discoveries based on ChMs of RGB stars is that 1G stars of most GCs are not chemically homogeneous (Milone et al., 2015b). As anticipated in Section 1.4, two main possibilities could explain the extended sequence of 1G stars:

- star-to-star chemical variations due to stellar evolution.
- chemical inhomogeneities in the pristine material from which the stars formed.

To disentangle between these two scenarios, in this Chapter I analyze the astro-photometric catalog derived for NGC 6362 using the procedures presented in Chapter 2. Specifically, Section 3.1 describes how the ChM was obtained for unevolved MS stars. Then, Section 3.2 illustrates the method adopted to constrain the chemical composition of 1G stars previously selected on the ChM. Finally, Section 3.3 introduces a possible way to disentangle between He or Fe variation based on isochrone fitting of SGB stars.

3.1 Chromosome Map

The ChM for NGC 6362 was built following the method introduced by Milone et al. (2015a) and then extensively used to study MPs in more than 60 Galactic GCs (e.g., Milone et al., 2017, 2018). The procedure, here applied to unevolved MS stars, is illustrated in Figure 3.1 and it was performed through the following steps:

1. **Retrieving the main sequence fiducial lines.** After selecting from the m_{F814W} vs. $m_{F275W} - m_{F814W}$ and m_{F814W} vs. $C_{F275W,F336W,F438W}$ CMDs the stars belonging to the MS ($18.0 < m_{F814W} < 20.0$), the latter was divided into a series of bins of size δm defined over a grid of points separated by fixed intervals of magnitude (δm/4). The fiducial lines that envelope MS stars in panels (a1) and (b1) of Figure 3.1 were determined calculating for each bin the 4^{th} and the 96^{th} percentile of the $m_{F275W} - m_{F814W}$ and $C_{F275W,F336W,F438W}$ color distributions together with the mean m_{F814W}. Specifically, the blue fiducial line corresponds to the 4^{th} percentile while the red one to the 96^{th} percentile. The fiducial lines are smoothed by means of boxcar averaging, where I replaced each point by the average of the three adjacent points.

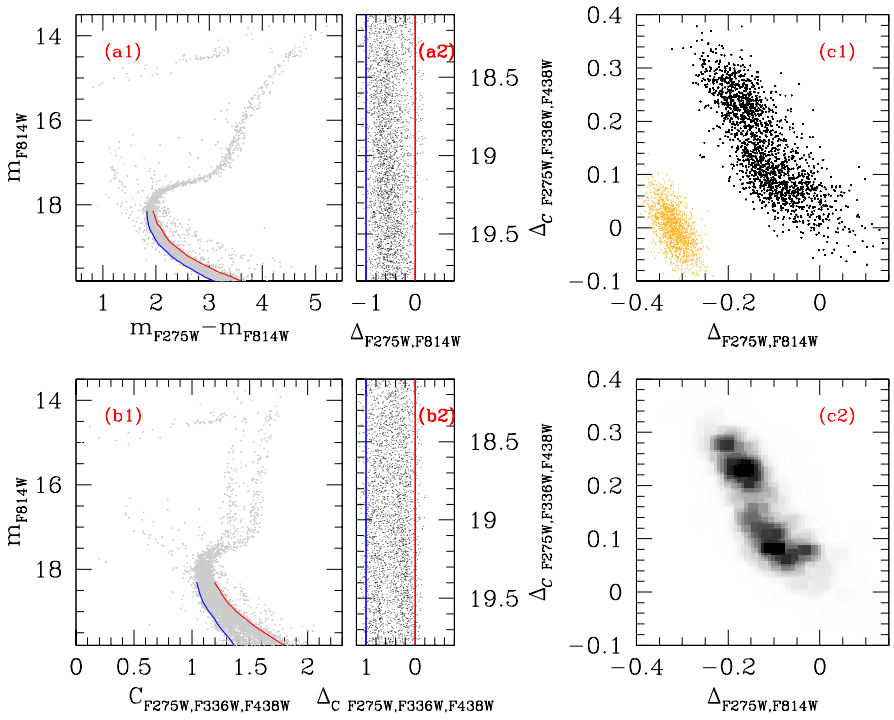

Figure 3.1: This figure illustrates the procedure used to derive the ChM for MS stars of NGC 6362. *Panels (a1) and (b1).* m_{F814W} vs. $m_{F275W} - m_{F814W}$ and m_{F814W} vs. $C_{F275W,F336W,F438W}$ CMDs. Blue and red fiducial lines mark the boundaries of the MS. *Panels (a2) and (b2).* 'Verticalized' m_{F814W} vs. $\Delta_{F275W,F814W}$ and m_{F814W} vs. $\Delta_{C\,F275W,F336W,F438W}$ diagrams for MS stars where the red and blue lines correspond to the 'verticalized' MS boundaries. *Panels (c1).* ChM of NGC 6362 obtained plotting $\Delta_{C\,F275W,F336W,F438W}$ against $\Delta_{F275W,F814W}$. The orange points in the bottom-left corner indicate the distribution of stars expected by observational errors only. *Panels (c2).* Hess diagram for stars in panel (c1).

2. **'Verticalization' of the CMDs.** The second step consisted in 'verticalizing' the m_{F814W} vs. $m_{F275W} - m_{F814W}$ and m_{F814W} vs. $C_{F275W,F336W,F438W}$ diagrams in order to transform the blue and red fiducial lines into vertical lines. The procedure is illustrated in panel (a2) and (b2) of Figure 3.1 and was obtained by calculating for each MS star:

$$\Delta_{F275W,F814W} = \frac{X - X_{\text{red fiducial}}}{X_{\text{red fiducial}} - X_{\text{blue fiducial}}} \tag{3.1}$$

$$\Delta_{C\,F275W,F336W,F438W} = \frac{Y - Y_{\text{red fiducial}}}{Y_{\text{red fiducial}} - Y_{\text{blue fiducial}}} \tag{3.2}$$

where $X = m_{F275W} - m_{F814W}$ and $Y = C_{F275W,F336W,F438W}$. Basically, the two quantities defined in Equation 3.1 and 3.2 are indicative, respectively, of the color and the pseudo-color distance from the corresponding red-fiducial lines.

3. **Building the ChM.** The ChM is obtained by plotting $\Delta_{C\,F275W,F336W,F438W}$ against $\Delta_{F275W,F814W}$ as represented in panel (c1) of Figure 3.1.

A visual inspection at the ChM of MS stars and its Hess diagram (panel (c2) of Figure 3.1) suggests that NGC 6362 hosts two main stellar populations, in close analogy with what was already observed for RGB stars (see, e.g., the ChM for RGB stars in Figure 4 of Milone et al., 2017). The 1G component was identified as the group of stars departing from the origin of the reference frame (red dots in top panel of Figure 3.2) while 2G stars define the sequence elongated towards large values of $\Delta_{C\,F275W,F336W,F438W}$ (blue dots in top panel of Figure 3.2).

First- and second-generation stars along the MS

Evidence that the distribution of MS stars in the ChM of NGC 6362 is not consistent with a simple stellar population is provided by the fact that the $\Delta_{F275W,F814W}$ and $\Delta_{C\,F275W,F336W,F438W}$ broadening of the observed points are much wider than the corresponding broadening of the observational errors (orange points in Figure 3.2), which are derived from AS tests.
To further demonstrate that the separation between 1G and 2G stars is intrinsic, I extended to NGC 6362 the method introduced by Anderson et al. (2009) to prove that the MS of the GC 47 Tuc hosts MPs. This method is based on the idea that if the MS broadening is due to observational errors alone, a star that is red (or blue) in a given photometric diagram has the same probability of being either red or blue in other diagrams built from a different dataset. Hence, two groups of selected blue and red stars should mix together with a consequent superimposition of their fiducial lines. On the contrary, separated fiducial lines would be the signature of distinct populations.
Specifically, I selected the samples of 1G and 2G stars previously identified on the ChM, in the m_{F606W} vs. $m_{F336W} - m_{F606W}$ and m_{F658N} vs. $m_{F438W} - m_{F658N}$ CMDs (bottom-left and right panel respectively in Figure 3.2). These groups of MS stars have been used to retrieve the corresponding fiducial lines. To do so, I used the same procedure described in the first step of the method for building the ChM with the only exception that, in this case, I calculated the median value for color and magnitude.
The fact that the fiducials of 1G and 2G stars are clearly separated in both CMDs

(see bottom panels of Figure 3.2) further demonstrates that the color distribution of 1G and 2G stars is intrinsic.

3.2 Chemical inhomogeneities among first-generation main sequence stars

The upper panel of Figure 3.2 clearly shows that the $m_{F275W} - m_{F814W}$ color distribution of 1G stars is much wider than that expected from observational uncertainties alone. Moreover, the 1G component exhibits wider color broadening than the 2G, as revealed by the kernel-density distributions of $\Delta_{F275W,F814W}$ of 1G and 2G stars (upper panel of Figure 3.2). Since 1G and 2G stars are affected by similar observational uncertainties, this fact demonstrates that the 1G is not chemically homogeneous.
To further investigate the color spread of MS stars, I extended the procedure described in the previous subsection to the 1G component. In a nutshell, I first identified two groups of 1G stars on the ChM, namely $1G_A$ and $1G_B$ (respectively magenta and green dots in Figure 3.3), with the criteria that each group comprises about half 1G stars. These two samples of stars were then plotted in two CMDs made with different filters, namely m_{F606W} vs. $m_{F336W} - m_{F606W}$ and m_{F658N} vs. $m_{F438W} - m_{F658N}$.
The results of this procedure are illustrated in the bottom panels of Figure 3.3. The fact that the fiducials of 1G and 2G stars are well separated in both the two CMDs reinforces the conclusion that 1G stars are not chemically homogeneous. Noticeable, it is the first time that this phenomenon is clearly observed among MS stars. The discovery of extended 1G sequence among unevolved MS stars roles out the possibility that chemical inhomogeneities are the result of stellar evolution and suggests that 1G stars of GCs are records of the chemical inhomogeneities in the primordial cloud where they formed at high redshift.

3.2.1 Insights from multi-band photometry of MS stars

To shed light on the physical phenomenon that is responsible for the color extension of the 1G sequence on the ChM, I applied to 1G stars of NGC 6362 the procedure by Milone et al. (2012c, 2018). This method consists in comparing the observed color distances between $1G_A$ and $1G_B$ stars with the predictions from appropriate isochrones that account for variations in light elements, helium and iron.
I started by selecting the groups of $1G_A$ and $1G_B$ stars in the m_{F814W} vs. $m_X - m_{F814W}$ CMDs, where X=F275W, F336W, F438W, F606W, F625W and F658N. Then, I derived the fiducial line of each sample of 1G stars by using the same procedure of Section 3.1. I defined a list of 5 reference points spaced by 0.25 magnitudes in the interval $18.75 \leq m_{F814W} \leq 19.75$. For each point, i, I calculated the $\Delta(m_X - m_{F814W})$ color difference between the fiducial of $1G_A$ and $1G_B$ stars. Results are shown in the lower panels of Figure 3.4 for X=F275W, F336W, F438W and F606W. Here, the fiducial lines are plotted in magenta and green for $1G_A$ and $1G_B$ stars, respectively. The $\Delta(m_X - m_{F814W})$ values derived for $m_{F814W,i} = 19.25$ (dotted horizontal line in bottom panels of Figure 3.4) are represented as filled circles in the upper-right panel of Figure 3.4. Clearly, the color separation between

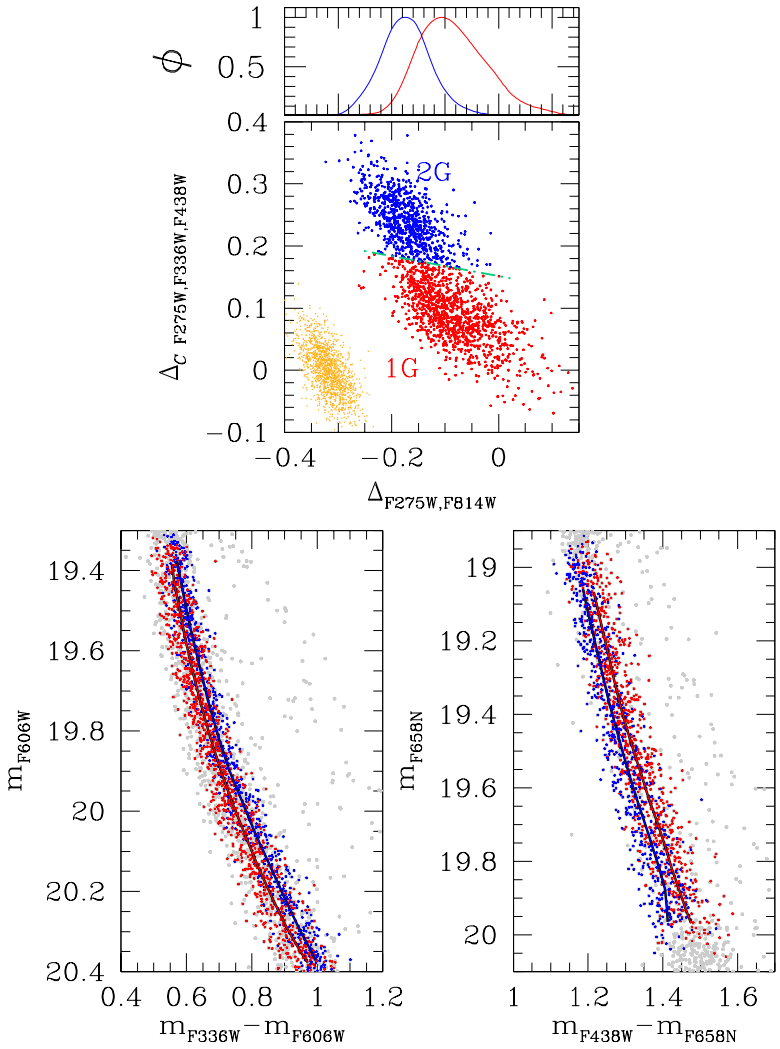

Figure 3.2: *Top.* ChM of MS stars in NGC 6362. 1G and 2G stars are colored red and blue respectively while the error distribution is represented by orange points on the bottom-left corner. The kernel-density distributions of 1G and 2G stars are plotted on the top panel. *Bottom.* m_{F606W} vs. $m_{F336W} - m_{F606W}$ (left) and m_{F658N} vs. $m_{F438W} - m_{F658N}$ (right) CMDs of MS stars in NGC 6362. The samples of 1G and 2G stars defined in the top panel are colored red and blue respectively while the fiducial lines of the 1G and 2G are superimposed on each CMD.

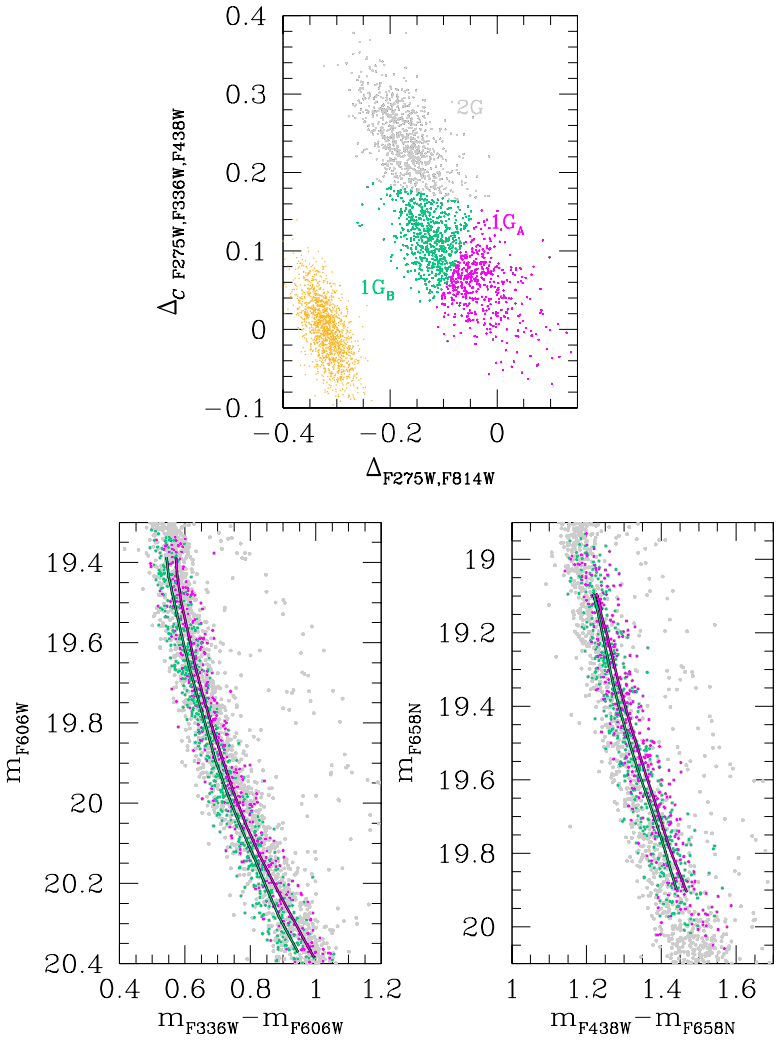

Figure 3.3: *Top.* ChM of MS stars in NGC 6362. The two samples of 1G stars ($1G_A$ and $1G_B$) are colored magenta and green respectively while the error distribution is represented by orange points. *Bottom.* m_{F606W} vs. $m_{F336W} - m_{F606W}$ (left) and m_{F658N} vs. $m_{F438W} - m_{F658N}$ (right) CMDs of MS stars in NGC 6362. The samples of 1G stars defined in the top panel are colored magenta and green respectively while the fiducial lines of the $1G_A$ and $1G_B$ are superimposed on each CMD.

$1G_A$ and $1G_B$ stars changes with the width of the color baseline reaching its maximum value for X=F275W.
The $\Delta(m_X - m_{F814W})$ values measured for each filter were then compared with the colors inferred from a grid of synthetic spectra with appropriate chemical compositions. To derive them, as a preliminary step, I estimated gravity and effective temperature corresponding to each point, *i*, by using the isochrones from the Dartmouth database (Dotter et al., 2008) and adopting the same age, reddening, distance modulus, metallicity and [α/Fe] listed in Dotter et al. (2010) for NGC 6362. For each reference point *i*, I then used the codes ATLAS12 (Kurucz, 2005; Castelli, 2005; Sbordone, 2005; Sbordone et al., 2007) and SYNTHE (Kurucz, 2005; Sbordone et al., 2007) to compute a reference synthetic spectrum and a grid of comparison spectra with different chemical compositions.
To calculate the reference one, I used the values of effective temperature, gravity and metallicity (Z) derived previously from the best-fit isochrone, together with primordial helium ($Y = 0.245 + 1.5 \times Z$), solar abundances of C and N, and [O/Fe] = 0.40. Comparison spectra, instead, were derived by using the same chemical composition as the reference one but changing the abundances of He, C, N, O and Fe. Specifically, in close analogy with was done by Milone et al. (2018), I simulated a grid of spectra enhanced in [N/Fe] up to 1.5 dex in steps of 0.1 dex, with [O/Fe] ranging from -0.2 to 0.4 in steps of 0.1 dex, [C/Fe] from -0.4 to 0.0 in steps of -0.1. Helium has been changed up to 0.33 and [Fe/H] by ± 0.2 dex. The atmospheric parameters, gravity and effective temperature, of the reference spectra have been derived from the Dartmouth isochrones (Dotter et al., 2008), accordingly with their metallicity and helium content. The color differences $\Delta(m_X - m_{F814W})^{synth}$ between the comparison and reference spectrum have been determined from the integration of each spectrum over the transmission curves of the seven HST filters used in this work for NGC 6362.
The comparison with the observed color distances between $1G_A$ and $1G_B$ stars allows to conclude that 1G stars share the same abundances of C, N and O and that, for a fixed luminosity, they exhibit internal variations in their effective temperature. This fact indicates that the color broadening of the 1G component is due either to He ($\Delta Y = 0.024$) or Fe (Δ[Fe/H] = 0.06 dex) variations, in agreement with both the main hypothesis discussed in Section 1.4.

3.3 Insights from the sub-giant branch

To disentangle the effect of helium and metallicity variations on the color extension of 1G stars, I introduce here a new approach, which is based on the SGB. Indeed, the isochrones from the Dartmouth database (Dotter et al., 2008) reveal that stellar populations with different helium abundances exhibit different SGB morphology compared to isochrones with different metallicities. This fact is illustrated in Figure 3.5 where I plotted the M_{F814W} vs. $M_{F438W} - M_{F814W}$ CMD for stellar populations reproducing the chemical composition of 1G stars in NGC 6362.
First of all, after selecting the sample of SGB stars from the m_{F814W} vs. $m_{F438W} - m_{F814W}$ CMD, I plotted them in the $m_{F336W} - m_{F438W}$ vs. $m_{F275W} - m_{F336W}$ two-color diagram. A visual inspection of the latter (represented in Figure 3.6) clearly reveals a bimodal distribution allowing to easily identify the 1G component as the group of stars at bluer colors on the left of the separator line (orange points in the right panel of Figure 3.6).

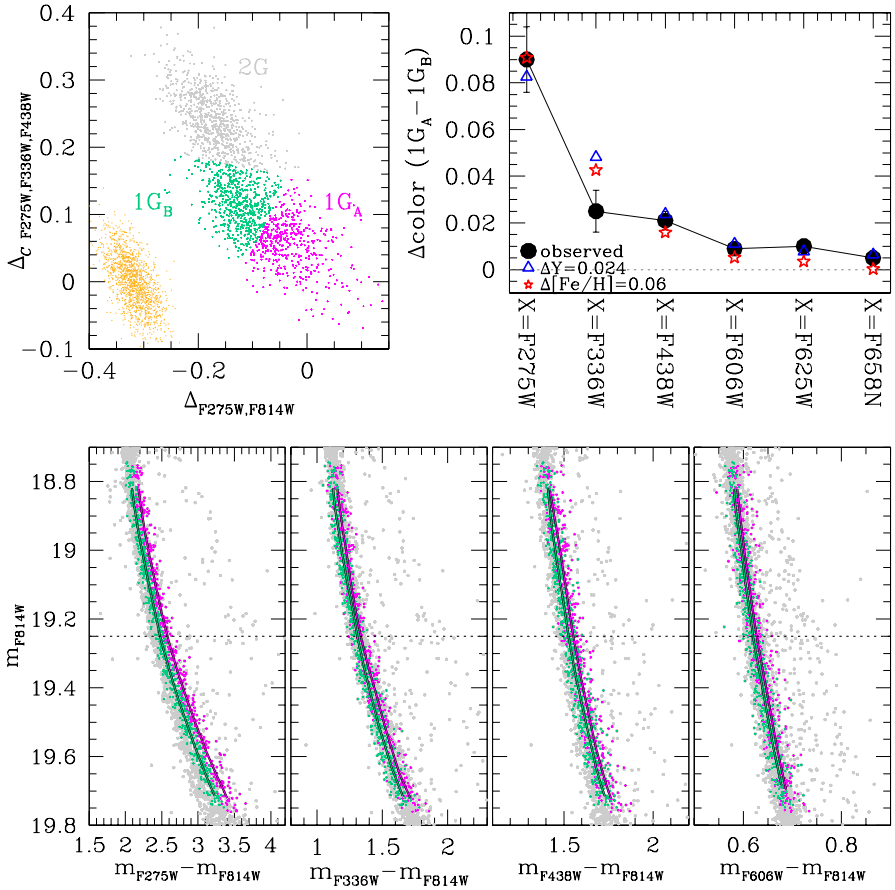

Figure 3.4: This figure illustrates the procedure used to derive the color differences between the two sub-groups of $1G_A$ and $1G_B$ stars. The upper-left panel reproduces the ChM plotted already in Figure 3.2 with the magenta and green points that identify $1G_A$ and $1G_B$ stars respectively. The lower panels show the $m_X - m_{F814W}$ CMDs where X=F275W, F336W, F438W and F606W (the same has been done for F625W and F658N filters) in which the fiducial lines obtained for $1G_A$ and $1G_B$ are plotted in magenta and green. The horizontal dotted line in each panel represents one of the reference magnitudes in F814W filter at which the color separation $\Delta(m_X - m_{F814W})$ has been calculated. Finally, the upper-right panel shows the comparison between the observed $\Delta(m_X - m_{F814W})$ with the colors inferred from synthetic spectra with different helium and iron abundances.

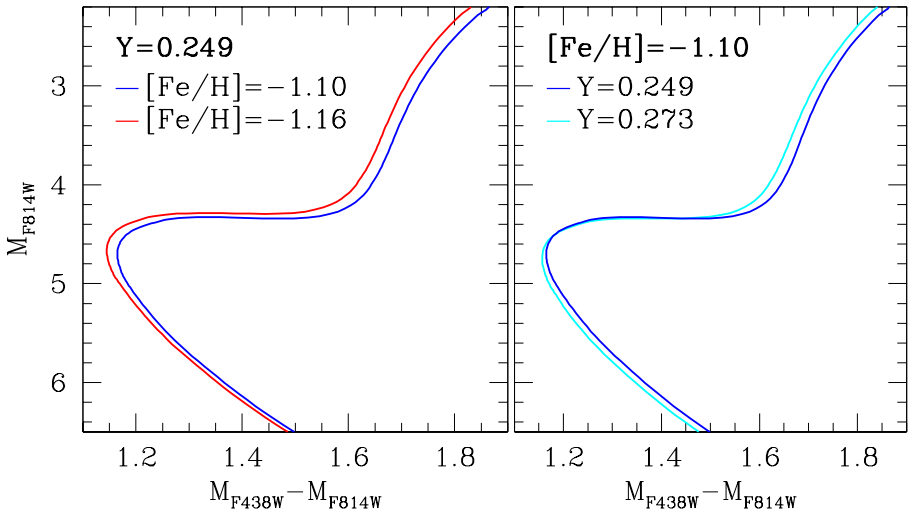

Figure 3.5: Isochrones with age of 12.5 Gyr and [α/Fe]=0.4 in the M_{F814W} vs. $M_{F438W} - M_{F814W}$ CMD. The blue isochrone has primordial helium abundance (Y=0.249) and [Fe/H]=−1.10 (from Dotter et al., 2010 while cyan and red isochrone are respectively enhanced in He by 0.024 (Y=0.273) and depleted in [Fe/H] by 0.06 ([Fe/H]=−1.16). The adopted helium and iron variations coincide with those inferred from the analysis of MS stars in Section 3.2.1.

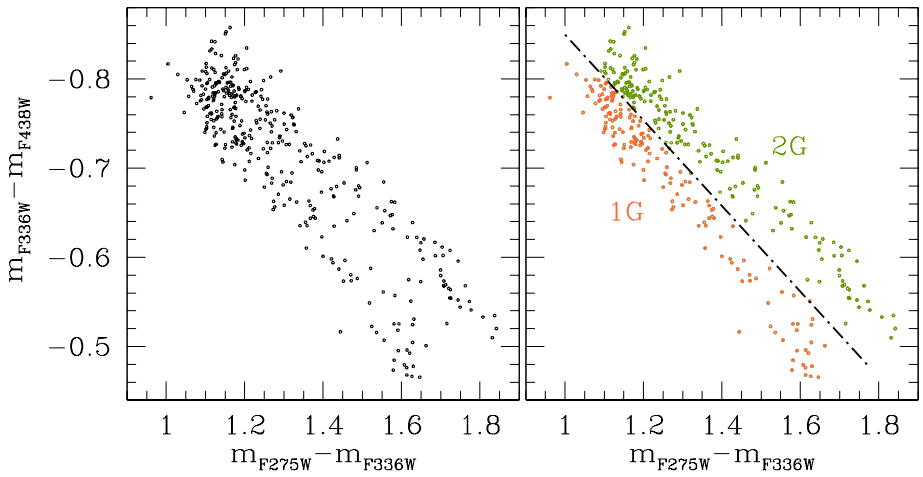

Figure 3.6: $m_{F336W} - m_{F438W}$ vs. $m_{F275W} - m_{F336W}$ two-color diagram for SGB stars. The dot-dashed line in the right panel empirically divides 1G and 2G stars, plotted respectively in orange and dark green.

The left panels of Figure 3.7, 3.8 reproduce respectively the m_{F275W} vs. $m_{F275W} - m_{F814W}$ and m_{F438W} vs. $m_{F438W} - m_{F814W}$ CMD where 1G stars previously selected on the SGB correspond to orange points. Additionally, I plotted the group of $1G_A$ and $1G_B$ MS stars identified on the ChM (magenta and green dots). Three isochrones from the Dartmouth database (Dotter et al., 2008) have been superimposed on each CMD adopting for all of them reddening of $E(B-V) = 0.67$, age of 12.5 Gyr and $[\alpha/Fe] = 0.4$ (age and $[\alpha/Fe]$ were derived from Dotter et al., 2010). Specifically, the blue isochrone has primordial helium abundance ($Y = 0.249$) and $[Fe/H] = -1.10$ (from Dotter et al., 2010) while cyan and red isochrones are respectively enhanced in He by 0.024 ($Y = 0.273$) and depleted in [Fe/H] by 0.06 ($[Fe/H] = -1.16$). Noticeably, the adopted helium and iron variations coincide with those inferred from the MS analysis in Section 3.2.1.
The isochrones with different helium and metallicity (red and cyan lines) are nearly coincident along the MS and exhibit similar color separations from the reference isochrone (blue line). This fact corroborates the conclusion that it is not possible to discriminate among helium and metallicity variations by using MS stars alone. On the contrary, isochrones with different Y and [Fe/H] exhibit different patterns along the SGB. A zoom on this region is presented in right panel of Figure 3.7, 3.8 respectively for the m_{F275W} vs. $m_{F275W} - m_{F814W}$ and m_{F438W} vs. $m_{F438W} - m_{F814W}$ CMD.
In order to quantitatively compare the observations with theoretical models, I introduced the following procedure. First of all, I computed the fiducial line of the 1G stars in the m_{F814W} vs. $m_{F438W} - m_{F814W}$ CMD (green line in upper left panel of Figure 3.9). Then, by subtracting to each 1G SGB star the color of the fiducial at the corresponding magnitude I derived $\Delta(m_{F438W} - m_{F814W})$. This quantity is plotted as a function of m_{F814W} in the upper right panel of Figure 3.9. To quantify the spread of the residuals, I calculated the standard deviation σ of the $\Delta(m_{F438W} - m_{F814W})$ distribution ($\sigma = 0.017$ mag) and $W^{SGB}_{F438W-F814W}$, namely the difference between the 90^{th} and the 10^{th} percentile ($W^{SGB}_{F438W-F814W} = 0.044$ mag). The latter, in particular, is more sensitive to possible outliers or tails of the distribution.
To compare the groups of 1G stars identified on the ChM, namely $1G_A$ and $1G_B$, with the simulations I generated the synthetic CMDs of three stellar populations based on the isochrones. Specifically, I generated a reference CMD of a stellar population with pristine helium content and $[Fe/H] = -1.10$, as derived from $1G_A$ (the corresponding isochrone is colored blue in Figure 3.7, 3.8). I also generated the synthetic CMDs (hereafter comparison CMDs) corresponding to the helium-enriched isochrone (cyan) and the iron-depleted one (red). I used the synthetic photometry to simulate two CMDs composed of stars in the reference and the comparison population. I assumed the same reference-to-comparison population ratio between $1G_A$ and $1G_B$ stars as the population ratio inferred from the ChM of MS stars. I included the binary fraction listed for NGC 6362 in Milone et al. (2012b).
The two m_{F814W} vs. $m_{F438W} - m_{F814W}$ CMDs have been compared with the observed one by extending the same analysis applied to observed SGB stars. Figure 3.9 represents the results of this procedure both for observed and simulated stars. Specifically, assuming helium variation alone, I found that the distribution of residuals, $\Delta(m_{F438W} - m_{F814W})$, has $\sigma = 0.018$ and $W^{SGB}_{F438W-F814W} = 0.046$, values that are comparable to the ones obtained for observed stars. In contrast, considering the simulated CMD reproducing the spread of the 1G component as due to iron

variation, I found higher values than the observed ones, respectively $\sigma = 0.025$ and $W^{SGB}_{F438W-F814W} = 0.061$.
This result suggests that helium variation of $Y \sim 0.024$ within the pristine material from which NGC 6362 formed is the main responsible for the extension of 1G stars in the ChM. Extending the innovative procedure proposed in this thesis to a large sample of clusters will be crucial to understand whether helium variation within 1G stars is a peculiarity of NGC 6362 or a common feature of all GCs.

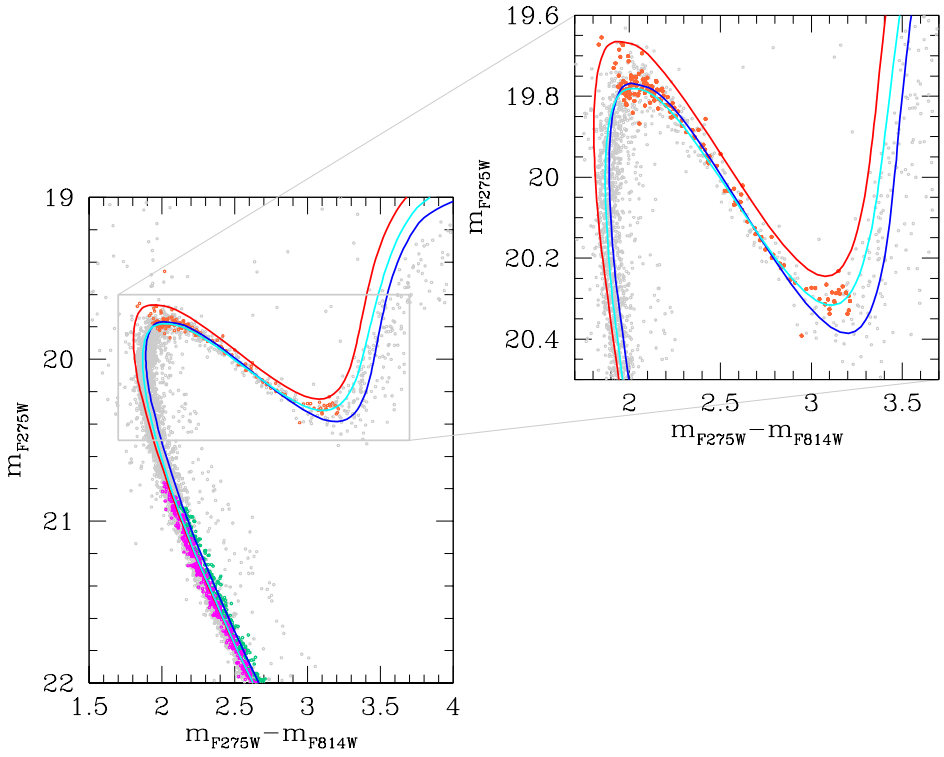

Figure 3.7: *Left.* m_{F275W} vs. $m_{F275W} - m_{F814W}$ CMD. $1G_A$ and $1G_B$ MS stars identified in Section 3.2.1 are colored magenta and green respectively while 1G SGB stars are represented by orange dots. Three isochrones from the Dartmouth database (Dotter et al., 2008) are superimposed on each CMD: the blue one is the best-fit isochrone for NGC 6362 with Y = 0.249 and [Fe/H] = −1.10 while the cyan and red ones are respectively enhanced in helium by 0.024 and depleted in iron by 0.06. *Right.* Same as in the left panel but zoomed around the SGB.

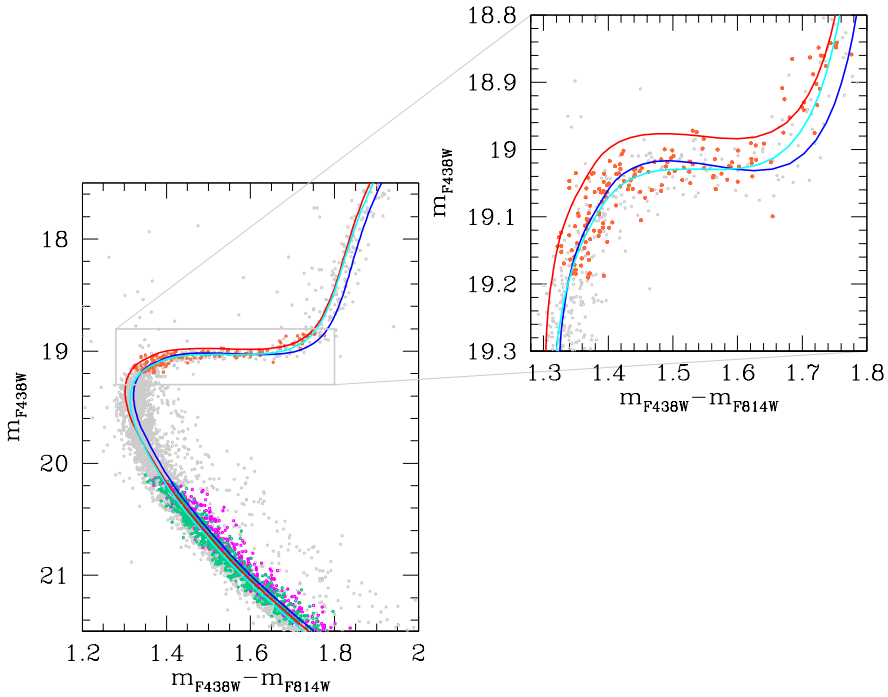

Figure 3.8: As in Figure 3.7 but for the m_{F438W} vs. $m_{F438W} - m_{F814W}$ CMD.

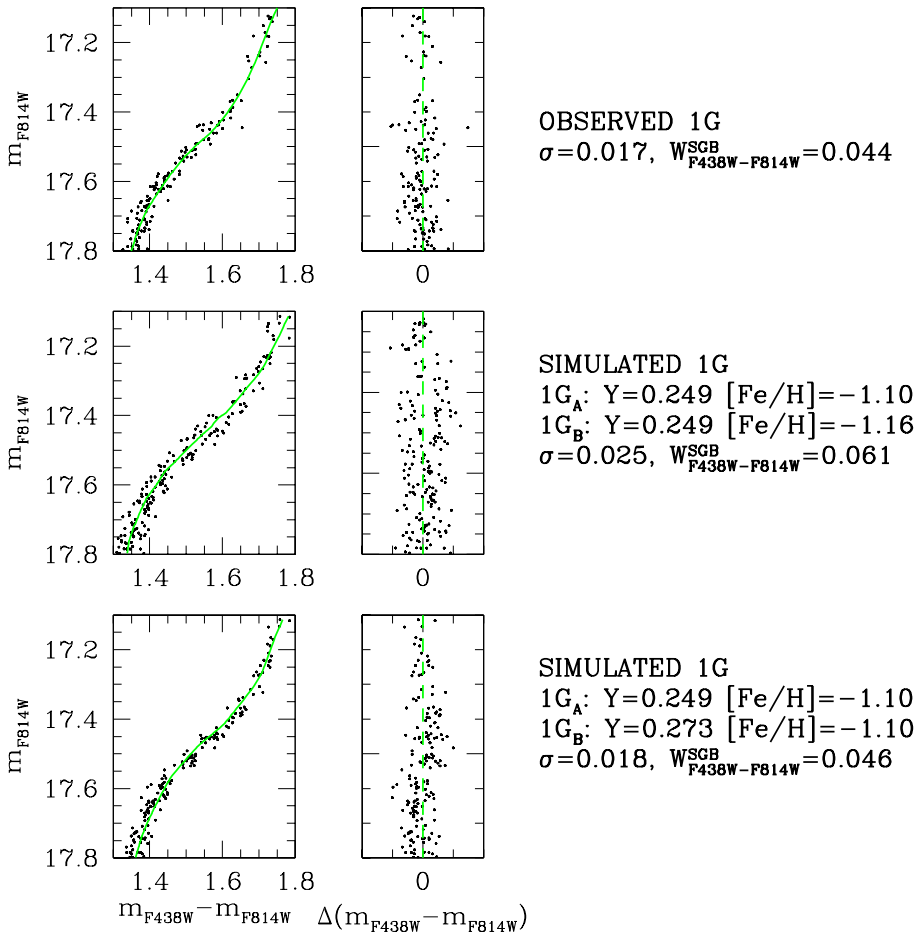

Figure 3.9: *Left.* m_{F814W} vs. $m_{F438W} - m_{F814W}$ CMD for observed (top) and simulated (middle and bottom) 1G stars belonging to the SGB. The fiducial line is overplotted in green. *Right.* The CMDs obtained after subtracting the fiducial line.

Chapter 4

Discussion and Conclusions

This thesis has demonstrated that the color extension of the 1G stars in the ChM of NGC 6362 is the signature of chemical inhomogeneities in the primordial cloud where stars formed at high redshift. Specifically, I found that 1G stars of NGC 6362 share constant C, N, O content but exhibit significant star-to-star variations either in helium or iron.
Starting from the result of NGC 6362, in this Chapter I exploit the colors of 1G RGB stars to infer the maximum abundance spread within the 1G of 55 Galactic GCs (Section 4.1). Moreover, I investigate the relations between the elemental spread and the main parameters of the host GC (Section 4.2). Finally, in Section 4.3 I summarize the results obtained and qualitatively constrain the environment where the proto-GCs formed in the early Universe.

4.1 Internal helium and iron variation among first-generation stars

In order to quantify the $\Delta_{\rm F275W,F814W}$ extension of 1G stars, Milone et al. (2017) have estimated the color width of 1G RGB stars of 57 Galactic GCs ($W^{\rm 1G}_{\rm F275W,F814W}$). This quantity is significantly larger than zero in most GCs demonstrating that the 1G component is not consistent with a simple stellar population.
By assuming that the 1G color spread is entirely due to helium variation, Milone et al. (2018) used the values of $W^{\rm 1G}_{\rm F275W,F814W}$ to derive the internal helium variation among 1G stars, $\Delta {\rm Y}_{\rm 1G}$. Results are plotted in left panel of Figure 4.1 representing the histogram distribution of $\Delta {\rm Y}_{\rm 1G}$ from which it can be seen that $\Delta {\rm Y}_{\rm 1G}$ ranges from ~ 0.00 to ~ 0.12 with values that changes dramatically from one cluster to another. In addition, it seems that $\Delta {\rm Y}_{\rm 1G}$ has a bimodal distribution with two main peaks around $\Delta {\rm Y}_{\rm 1G} \sim 0.04$ and ~ 0.08.
In this thesis, I derived the internal [Fe/H] variation in 55 GCs, $\Delta {\rm [Fe/H]}_{\rm 1G}$, by assuming that iron variation is the only factor leading to the 1G color spread. To do this, I exploited the relation between the ${\rm m_{F275W} - m_{F814W}}$ color and the metallicity from Dotter et al. (2008) to transform the $W^{\rm 1G}_{\rm F275W,F814W}$ ChM widths into iron variations. Results are illustrated in the left panel of Figure 4.2 where the histogram distribution of $\Delta {\rm [Fe/H]}_{\rm 1G}$ is plotted. As in the case of helium variation, I found that the internal iron variation within the 1G component changes dramat-

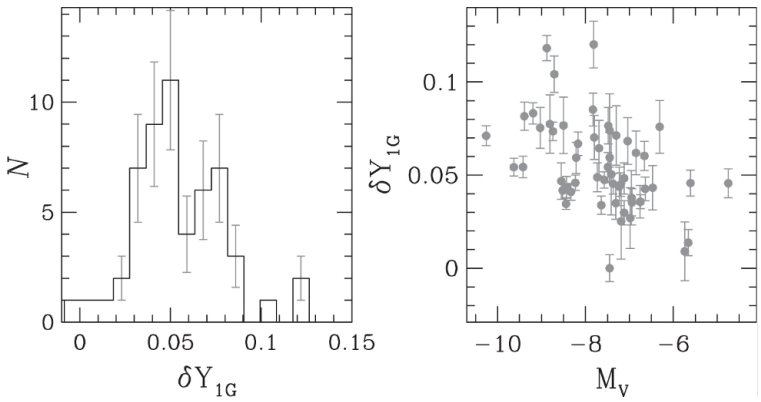

Figure 4.1: *Left.* Histogram distribution of internal helium variation among 1G stars (ΔY_{1G}) for the clusters studied in Milone et al. (2018). *Right.* Relation between ΔY_{1G} and the absolute visual magnitude (M_V) of the host GC. Figure from Milone et al. (2018).

ically from one cluster to another ranging from ~ 0.00 to ~ 0.30 with an average value of $\Delta[Fe/H]_{1G} \sim 0.12$. Moreover, the histogram distribution presents some hints for two main peaks, one centered around the mean value while the other at a slightly smaller value, namely $\Delta[Fe/H]_{1G} \sim 0.07$. The analogies in the distribution of ΔY_{1G} and $\Delta[Fe/H]_{1G}$ are confirmed by the strong correlation between the two quantities for which the Spearman's rank coefficient, R_S, is equal to 0.8 and the p-value is less than 0.001 (right panel of Figure 4.2).
The value of $\Delta[Fe/H]_{1G}$ found for each cluster together with the associated error are listed in Table 4.1 where, for completeness, I also include $W^{1G}_{F275W,F814W}$ and ΔY_{1G} (Milone et al., 2017, 2018).

4.2 Correlation with globular cluster parameters

In the following, I investigate the correlations between the internal helium and iron variations among 1G stars (ΔY_{1G} and $\Delta[Fe/H]_{1G}$ respectively) and the main parameters of the host GC. Such parameters include:

- Metallicity ([Fe/H]), absolute visual magnitude (M_V), ellipticity (ϵ), central concentration (c), central stellar density (ρ_0) and central surface brightness (μ_V) derived from the 2010 version of Harris catalog (Harris, 1996).
- Present-day (M) and initial mass (M_{in}) of the host cluster, central escape velocity (v_{esc}), central velocity dispersion (σ_v), core density (ρ_c) and core relaxation time at half mass (τ_{hm}) taken from Baumgardt and Hilker (2018). The mass of the 1G is obtained using the fraction of 1G stars calculated by Milone et al. (2017).
- GC ages derived respectively from Marin-Franch et al. (2009, MF09), Dotter et al. (2010, D10), VandenBerg et al. (2013, V13) and Tailo et al. (2020, T20).
- The fraction of binary stars in GCs taken from Milone et al. (2012b) as measured within the cluster core (f^C_{bin}), in the region between the core and the

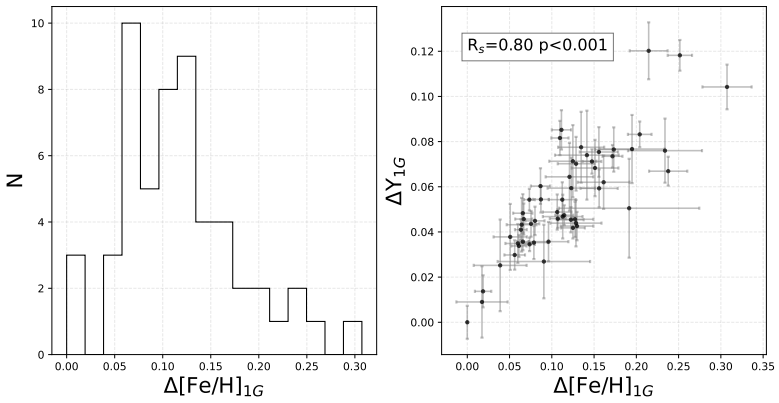

Figure 4.2: *Left.* Histogram distribution of internal iron variation among 1G stars (Δ[Fe/H]$_{1G}$) obtained for 55 Galactic GCs. *Right.* Relation between the values of internal helium variation among 1G stars (ΔY_{1G}) obtained by Milone et al. (2018) and the corresponding results for iron obtained in this work using the same procedure. The Spearman's rank correlation coefficient together with the associated p-value are reported in the upper-left box.

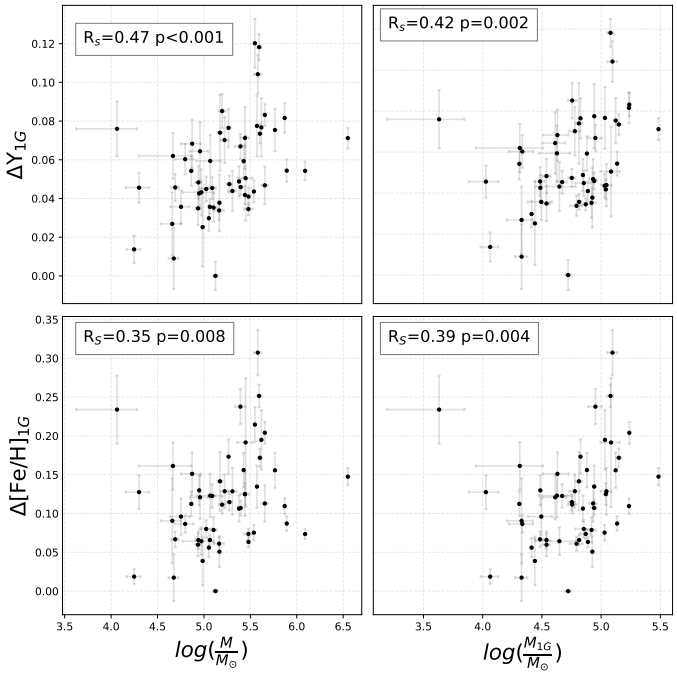

Figure 4.3: *Top.* Correlation between internal helium variation among 1G stars (ΔY_{1G}) and the present-day mass of the host cluster (left) and the 1G (right). *Bottom.* Correlation between internal iron variation among 1G stars (Δ[Fe/H]$_{1G}$) and the present-day mass of the host cluster (left) and the 1G (right). In both panels the value of the Spearman's rank coefficient and the associated p-value are reported.

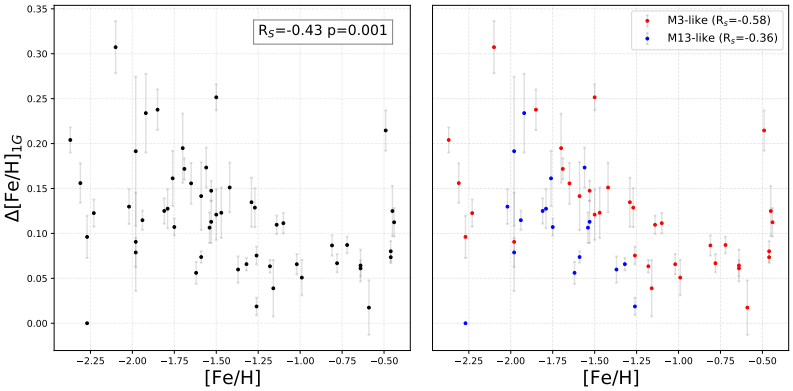

Figure 4.4: *Left.* Correlation between internal iron variation among 1G stars (Δ[Fe/H]$_{1G}$) and metallicity ([Fe/H]). *Right.* Same as left panel but highlighting the separation between M 3- (red dots) and M 13-like objects (blue dots).

half-mass radius ($f_{\rm bin}^{\rm C-HM}$) and beyond the half-mass radius ($f_{\rm bin}^{\rm oHM}$).

The results of the correlations between ΔY_{1G}, Δ[Fe/H]$_{1G}$ and the cluster parameters are listed in Table 4.2 where for each pair of analyzed quantities the Spearman's rank coefficient (R_S), the corresponding p-value, indicative of the correlation significance, and the number of degrees of freedom are reported.
I confirmed a mild anti-correlation ($R_S = -0.51$) between the internal helium variation among 1G stars and the cluster absolute luminosity (see also Milone et al., 2018). In addition, I found that ΔY_{1G} shows mild correlations also with the present-day mass of the host cluster ($R_S = 0.47$) and of the 1G ($R_S = 0.42$). When considering the initial mass of the cluster, instead, the correlation becomes less significant ($R_S = 0.31$). The same trend is also followed by the internal iron variation among 1G stars but with value of R_S that generally are lower than the one obtained for ΔY_{1G}. No other significant correlations with cluster parameters have been found ($f_{\rm bin}^{\rm C}$ shows a mild anti-correlation both with ΔY_{1G} and Δ[Fe/H]$_{1G}$ but it reflects the relation with the mass) except for the relation between Δ[Fe/H]$_{1G}$ and [Fe/H] ($R_S = -0.43$), depicted in the left panel of Figure 4.4 where it can be seen that, on average, more metal-poor clusters are characterized by higher values of Δ[Fe/H]$_{1G}$. The relations between the elemental spread and the present-day mass of the host GC and the 1G are presented in Figure 4.3.

M 3- and M 13-like clusters

To investigate further the relations between ΔY_{1G} and Δ[Fe/H]$_{1G}$ and the host cluster parameters, I divided GCs in two categories according to the associated value of L_1. This parameter, introduced by Milone et al. (2014b) to investigate the so-called second parameter problem linked to HB morphology, is defined as the color difference between the RGB and the reddest part of the HB. Specifically, by adopting the same nomenclature by Tailo et al. (2020), I defined M 3-like GCs with $L_1 \leq 0.35$, which mostly include GCs having red HBs, and M 13-like GCs with $L_1 > 0.35$ in which the red HB stars are missing.

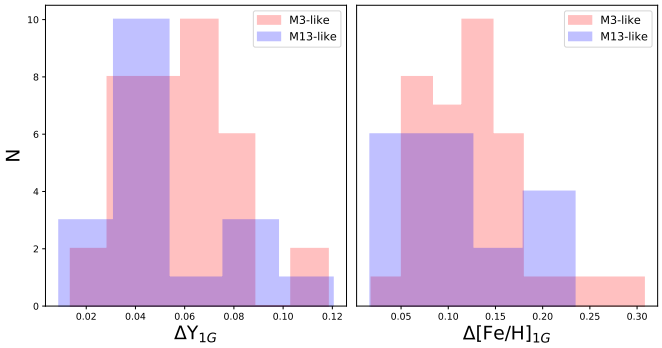

Figure 4.5: *Left.* Histogram distribution of internal helium variation among 1G stars (ΔY_{1G}) for M 3-(red) and M 13-like clusters (blue). *Right.* Same as left panel but for internal iron variation among 1G stars ($\Delta[Fe/H]_{1G}$).

Figure 4.5 shows the histogram distribution of ΔY_{1G} (left) and $\Delta[Fe/H]_{1G}$ (right) highlighting the separation between M 3- (red) and M 13-like (blue) clusters. Intriguingly, the 1G stars of GCs with the red HB exhibit wider abundance scatter than in GCs with the blue HB alone. This fact is also evident in Figure 4.6 where the relation between ΔY_{1G} and $\Delta[Fe/H]_{1G}$ is illustrated for the two samples of M 3- (red dots) and M 13-like clusters (blue dots).
Moreover, analyzing the two samples of clusters separately, I found that they behave in an opposite way: indeed, internal helium and iron variations within the 1G of M 3-like GCs show a mild correlation with both the present-day mass of the cluster and of the 1G while the correspondent variations in M 13-like are characterized by no correlation at all. These relations are illustrated in top and bottom panels of Figure 4.7 respectively for ΔY_{1G} and $\Delta[Fe/H]_{1G}$. Here, M 3-like clusters correspond to red dots while M 13-like objects to blue ones. The same trend is also found for the relation between $\Delta[Fe/H]_{1G}$ and metallicity, as illustrated in the right panel of Figure 4.4. Moreover, M 3-like GCs with $[Fe/H] < -1.00$ tend to have higher internal iron variation than M 13-like objects with the same metallicity.

4.3 Summary and Conclusions

Since Galactic GCs are among the most-ancient objects of the Galaxy, their 1G stars provide the unique opportunity to trace the chemical composition of the primordial clouds where they formed at high redshift. To this aim, I exploited high-precision multi-band HST photometry of the Galactic GC NGC 6362. The photometry has been derived from archive images collected through the F275W, F336W, F438W filters of UVIS/WFC3 and the F606W, F625W, F658N and F814W filters of WFC/ACS.
The main results on NGC 6362 of this thesis can be summarized as follows:

- I combined the $C_{F275W,F336W,F438W}$ pseudo-color and the $m_{F275W} - m_{F814W}$ color to build the ChM of MS stars. The latter shows two well separated groups of stars that correspond to the first and second generation (1G and 2G). In close analogy with what was observed for RGB stars, I found that the

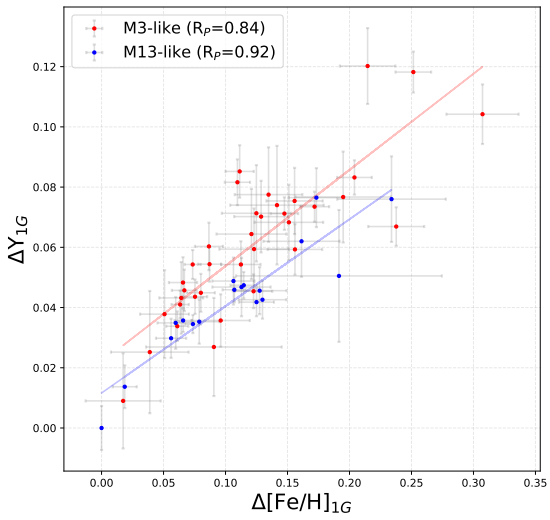

Figure 4.6: Same as right panel of Figure 4.2 but highlighting the separation between M 3-(red dots) and M 13-like objects (blue dots). Red and blue line are the best-fit line obtained by means of least squares for M 3- and M 13-like clusters respectively.

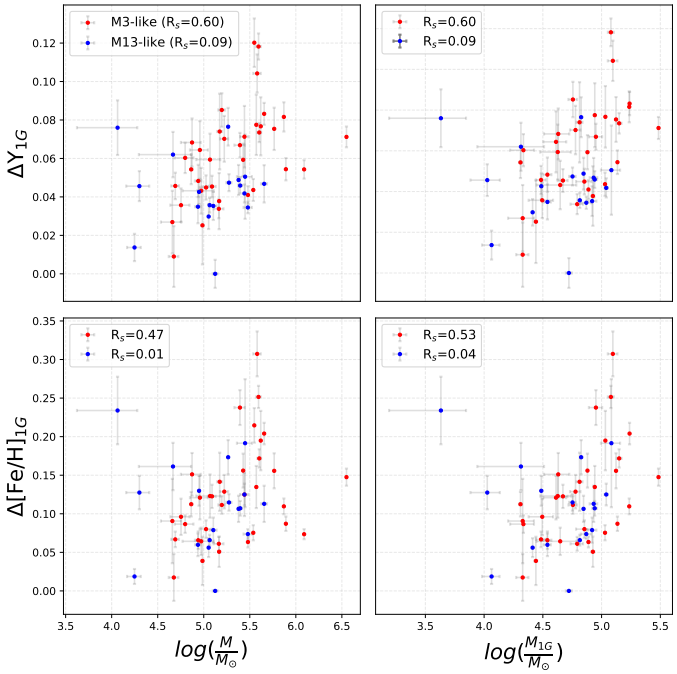

Figure 4.7: Same as Figure 4.3 but highlighting the separation between M 3- (red dots) and M 13-like objects (blue dots).

distribution of 1G MS stars is wider than observational errors thus demonstrating that 1G stars are not chemically homogeneous. Remarkably, this is the first time that this phenomenon is clearly observed among unevolved stars. The discovery of extended 1G sequence among unevolved MS stars rules out the possibility that chemical inhomogeneities are the result of stellar evolution. Therefore, 1G stars of GCs are records of the chemical inhomogeneities of the primordial cloud where they formed at high redshift.

- To investigate chemical variations within the 1G component of NGC 6362, I compared multi-band HST photometry of MS stars with colors derived from grids of synthetic spectra with appropriate chemical compositions. I found that 1G stars have constant C, N, O content and that, for a fixed luminosity, 1G stars exhibit internal variation in their effective temperature. This fact indicates that the color broadening of the 1G is due either to helium (Y = 0.024) or iron ([Fe/H] = 0.06 dex) variation.

- To disentangle between helium and iron variation within the 1G component, I introduced a possible method based on isochrones fitting of SGB stars. Results for NGC 6362 suggest that helium variation is responsible for the observed 1G spread on the ChM. However, since this analysis is limited to a single cluster, it is mandatory to extend the method of this thesis to a large sample of cluster to understand whether helium variations are common features of 1G stars in all GCs.

To investigate the 1G sequences in a large sample of clusters, I exploited the results from Milone et al. (2017) on 55 Galactic GCs. In this analysis, I considered both possibilities that the 1G color spread is due to helium and metallicity variations.

- I exploited the F275W−F814W color extension of 1G RGB stars to infer the internal iron variation within the 1G of 55 Galactic GCs. To do this, I assumed that the 1G color extension is entirely due to iron. I found that Δ[Fe/H]$_{1G}$ changes dramatically from one cluster to another ranging from ~ 0.00 to ~ 0.30 with an average value of Δ[Fe/H]$_{1G} \sim 0.12$.

- I investigated the relations between internal helium and iron variations among 1G stars and the main parameters of the host GC. I found that both ΔY_{1G} and Δ[Fe/H]$_{1G}$ show a mild correlation with GC mass and the 1G mass. Additionally, iron variation within the 1G mildly correlates also with the metallicity of the host cluster.

- Intriguingly, the 1G stars of those GCs with the red HB (M 3-like) exhibit wider abundance scatter than in M 13-like GCs with the same metallicity. Moreover, only M 3-like GCs exhibit the correlation between internal iron and helium variation and cluster mass.

The possibility that 1G stars have an internal spread in the overall metallicity would suggest that GCs have been able to retain a small amount of material polluted by SNe. On the other hand, if He is responsible for the color broadening of the 1G component on the ChM, a nucleosynthesis process occurred in stars that produced a helium variation without changing the C, N, O content. To explain a pure helium spread among 1G stars, Milone et al. (2018) discussed some scenarios associated to pp-chain reactions but none appears to work. Alternatively, an internal helium

spread within the 1G could be associated to exotic phenomena affecting the gas at very high redshift. A possible explanation has been recently suggested by Arbey et al. (2020) who demonstrate that abundance anomalies may generate in patches of the Universe characterized by extremely high baryon-to-photon ratio. Such dense regions possibly derive from large primordial isocurvatures perturbations that are thought to collapse forming primordial black holes (PBHs). The PBH hypothesis has an important consequence: for any plausible initial conditions, it is likely to have many uncollapsed isocurvature fluctuations ('failed' PBHs) that might have later formed stars that retained a memory of inhomogeneous Big Bang Nucleosynthesis (BBN). Searching for stellar relics that are in effect failed PBHs would be extremely challenging at the present epoch because of the dilution caused by several phenomenons, as for example mass mixing on galactic scales or stellar evolution, but it cannot be excluded since initial signals of inhomogenous BBN could still survive as anomalous primordial abundances visible in a small fraction of the oldest stars. Specifically, signatures of a high barion-to-photon ratio include elevate helium variations.
Large abundance spreads (both in helium and iron), as the ones measured for M 3-like GCs, are representative of extended regions with low gas density. Consequently, the fact that M 13-like GCs have more compact 1G sequence on the ChM (see Milone et al., 2017) may indicate that they formed in high-density environment where the material homogenized. This scenario is consistent with the results found by Tailo et al. (2020) according to which 1G stars of M 13-like GCs loose more mass than the 1G stars of M 3-like GCs with the same metallicity. Analogously, extremely dense environments are required to potentially justify the fact that in some GCs (as for example the case of the cluster studied in this work, NGC 6362) the 2G component shows a less extended color broadening than the 1G on the ChM. This explanation would exclude a scenario in which 1G and 2G stars are coeval and the chemical variations are due to mass accreted onto existing low-mass stars.

Cluster ID	$W^{1G}_{m_{F275W}-m_{F814W}}$	ΔY_{1G}	Δ[Fe/H]$_{1G}$	Group
NGC 0104	0.216 ± 0.023	0.054 ± 0.006	0.087 ± 0.009	M 3-like
NGC 0288	0.075 ± 0.008	0.036 ± 0.004	0.066 ± 0.007	M 13-like
NGC 0362	0.092 ± 0.012	0.044 ± 0.006	0.075 ± 0.010	M 3-like
NGC 1261	0.148 ± 0.025	0.070 ± 0.012	0.129 ± 0.022	M 3-like
NGC 1851	0.090 ± 0.010	0.041 ± 0.005	0.063 ± 0.007	M 3-like
NGC 2298	0.139 ± 0.026	0.076 ± 0.014	0.234 ± 0.046	M 13-like
NGC 2808	0.183 ± 0.017	0.082 ± 0.008	0.110 ± 0.010	M 3-like
NGC 3201	0.150 ± 0.040	0.074 ± 0.020	0.142 ± 0.038	M 3-like
NGC 4590	0.065 ± 0.008	0.045 ± 0.006	0.123 ± 0.015	M 3-like
NGC 4833	0.126 ± 0.012	0.067 ± 0.006	0.238 ± 0.023	M 3-like
NGC 5024	0.169 ± 0.016	0.104 ± 0.010	0.307 ± 0.029	M 3-like
NGC 5053	0.049 ± 0.012	0.036 ± 0.009	0.091 ± 0.024	M 3-like
NGC 5139	0.146 ± 0.011	0.071 ± 0.005	0.148 ± 0.011	M 3-like
NGC 5272	0.244 ± 0.014	0.118 ± 0.007	0.252 ± 0.015	M 3-like
NGC 5286	0.146 ± 0.010	0.073 ± 0.005	0.172 ± 0.012	M 3-like
NGC 5466	0.048 ± 0.029	0.027 ± 0.016	0.091 ± 0.055	M 3-like
NGC 5897	0.081 ± 0.019	0.044 ± 0.010	0.127 ± 0.030	–
NGC 5904	0.163 ± 0.033	0.078 ± 0.016	0.135 ± 0.027	M 3-like
NGC 5927	0.631 ± 0.066	0.120 ± 0.013	0.215 ± 0.022	M 3-like
NGC 5986	0.070 ± 0.006	0.035 ± 0.003	0.074 ± 0.006	M 13-like
NGC 6093	0.090 ± 0.008	0.046 ± 0.004	0.107 ± 0.010	M 13-like
NGC 6101	0.063 ± 0.013	0.035 ± 0.007	0.079 ± 0.016	M 13-like
NGC 6121	0.056 ± 0.045	0.025 ± 0.020	0.039 ± 0.031	M 3-like
NGC 6144	0.121 ± 0.023	0.062 ± 0.012	0.161 ± 0.031	M 13-like
NGC 6171	0.115 ± 0.020	0.048 ± 0.008	0.066 ± 0.011	M 3-like
NGC 6205	0.096 ± 0.020	0.047 ± 0.010	0.113 ± 0.024	M 13-like
NGC 6218	0.073 ± 0.018	0.035 ± 0.009	0.060 ± 0.015	M 13-like
NGC 6254	0.156 ± 0.020	0.077 ± 0.010	0.173 ± 0.022	M 13-like
NGC 6304	0.371 ± 0.083	0.071 ± 0.016	0.125 ± 0.028	M 3-like
NGC 6341	0.078 ± 0.011	0.059 ± 0.008	0.156 ± 0.022	M 3-like
NGC 6352	0.193 ± 0.053	0.043 ± 0.012	0.064 ± 0.018	M 3-like
NGC 6362	0.093 ± 0.036	0.038 ± 0.015	0.051 ± 0.020	M 3-like
NGC 6366	0.043 ± 0.075	0.009 ± 0.016	0.017 ± 0.030	M 3-like
NGC 6397	0.074 ± 0.011	0.043 ± 0.006	0.130 ± 0.019	M 13-like
NGC 6441	0.283 ± 0.025	0.054 ± 0.005	0.074 ± 0.007	M 3-like
NGC 6496	0.234 ± 0.033	0.045 ± 0.006	0.080 ± 0.011	M 3-like
NGC 6535	0.088 ± 0.015	0.046 ± 0.008	0.128 ± 0.022	M 13-like
NGC 6541	0.080 ± 0.009	0.042 ± 0.005	0.125 ± 0.014	M 13-like
NGC 6584	0.133 ± 0.031	0.064 ± 0.015	0.121 ± 0.028	M 3-like
NGC 6624	0.282 ± 0.040	0.054 ± 0.008	0.112 ± 0.016	M 3-like
NGC 6637	0.151 ± 0.022	0.034 ± 0.005	0.061 ± 0.009	M 3-like
NGC 6652	0.207 ± 0.027	0.060 ± 0.008	0.087 ± 0.011	M 3-like
NGC 6656	0.152 ± 0.030	0.077 ± 0.015	0.195 ± 0.039	M 3-like
NGC 6681	0.060 ± 0.013	0.030 ± 0.007	0.056 ± 0.012	M 13-like
NGC 6717	0.029 ± 0.015	0.014 ± 0.007	0.019 ± 0.010	M 13-like
NGC 6723	0.195 ± 0.020	0.085 ± 0.009	0.111 ± 0.011	M 3-like
NGC 6752	0.100 ± 0.016	0.049 ± 0.008	0.106 ± 0.017	M 13-like
NGC 6779	0.090 ± 0.039	0.051 ± 0.022	0.192 ± 0.083	M 13-like
NGC 6809	0.086 ± 0.008	0.047 ± 0.004	0.115 ± 0.011	M 13-like
NGC 6838	0.165 ± 0.025	0.046 ± 0.007	0.067 ± 0.010	M 3-like
NGC 6934	0.123 ± 0.028	0.059 ± 0.014	0.123 ± 0.028	M 3-like
NGC 6981	0.142 ± 0.026	0.068 ± 0.013	0.151 ± 0.028	M 3-like
NGC 7078	0.102 ± 0.007	0.083 ± 0.006	0.204 ± 0.014	M 3-like
NGC 7089	0.151 ± 0.022	0.075 ± 0.011	0.156 ± 0.023	M 3-like
NGC 7099	0.000 ± 0.010	0.000 ± 0.007	0.000 ± 0.020	M 13-like

Table 4.1: This table lists for each cluster the intrinsic $m_{F275W} - m_{F814W}$ color width of 1G ($W^{1G}_{m_{F275W}-m_{F814W}}$) derived by Milone et al. (2017) together with the internal helium (ΔY_{1G}) and iron (Δ[Fe/H]$_{1G}$) variations among 1G stars estimated respectively in Milone et al. (2018) and in this work. The GC group (using the same nomenclature as in Tailo et al., 2020) is also reported in the last column.

Parameter	ΔY_{1G}	$\Delta[Fe/H]_{1G}$
Age (MF09)	$-0.20, 0.138, 52$	$-0.16, 0.247, 52$
Age (D10)	$-0.09, 0.532, 53$	$0.23, 0.098, 53$
Age (V13)	$-0.14, 0.328, 48$	$0.15, 0.286, 48$
Age (T20)	$-0.12, 0.415, 44$	$0.11, 0.476, 44$
[Fe/H]	$0.01, 0.962, 53$	$-0.43, < 0.001, 53$
$\log(M/M_\odot)$	$0.47, < 0.001, 53$	$0.35, 0.008, 53$
$\log(M_{in}/M_\odot)$	$0.31, 0.023, 53$	$0.17, 0.213, 53$
$\log(M_{1G}/M_\odot)$	$0.42, 0.002, 50$	$0.39, 0.004, 50$
M_V	$-0.50, < 0.001, 53$	$-0.36, 0.007, 53$
ϵ	$0.12, 0.408, 51$	$0.23, 0.091, 51$
f_{bin}^{C}	$0.37, 0.027, 33$	$0.44, 0.008, 33$
f_{bin}^{C-HM}	$0.22, 0.143, 44$	$0.25, 0.094, 44$
f_{bin}^{oHM}	$0.09, 0.575, 39$	$0.05, 0.742, 39$
c	$0.15, 0.272, 53$	$0.06, 0.656, 53$
$\log(\tau_{hm})$	$0.23, 0.096, 53$	$0.31, 0.020, 53$
ρ_0	$0.09, 0.5, 53$	$0.06, 0.658, 53$
μ_V	$0.20, 0.152, 53$	$0.02, 0.884, 53$
$\log(\rho_c)$	$0.02, 0.881, 53$	$-0.08, 0.547, 53$
σ_v	$0.37, 0.005, 53$	$0.19, 0.174, 53$
v_{esc}	$0.36, 0.006, 53$	$0.19, 0.175, 53$

Table 4.2: Correlation of the internal helium (ΔY_{1G}) and iron ($\Delta[Fe/H]_{1G}$) variations among 1G stars against 20 GC parameters. For each parameter the Spearman's rank correlation coefficient is reported together with the associated p-value, indicative of the significance of the relation, and the number of freedom degrees.

Bibliography

J. Anderson and I. R. King. Toward high-precision astrometry with wfpc2. i. deriving an accurate point-spread function. *Publications of the Astronomical Society of the Pacific*, 112(776):1360, 2000.

J. Anderson and I. R. King. PSFs, Photometry, and Astronomy for the ACS/WFC. Instrument Science Report ACS 2006-01, Feb. 2006.

J. Anderson, I. R. King, H. B. Richer, G. G. Fahlman, B. M. Hansen, J. Hurley, J. S. Kalirai, R. M. Rich, and P. B. Stetson. Deep advanced camera for surveys imaging in the globular cluster ngc 6397: reduction methods. *The Astronomical Journal*, 135(6):2114, 2008a.

J. Anderson, A. Sarajedini, L. R. Bedin, I. R. King, G. Piotto, I. N. Reid, M. Siegel, S. R. Majewski, N. E. Paust, A. Aparicio, et al. The acs survey of globular clusters. v. generating a comprehensive star catalog for each cluster. *The Astronomical Journal*, 135(6):2055, 2008b.

J. Anderson, G. Piotto, I. King, L. Bedin, and P. Guhathakurta. Mixed populations in globular clusters: Et tu, 47 tuc? *The Astrophysical Journal Letters*, 697(1): L58, 2009.

A. Arbey, J. Auffinger, and J. Silk. Stellar signatures of inhomogeneous big bang nucleosynthesis. *Physical Review D*, 102(2):023503, 2020.

N. Bastian, H. Lamers, S. de Mink, S. Longmore, S. Goodwin, and M. Gieles. Early disc accretion as the origin of abundance anomalies in globular clusters. *Monthly Notices of the Royal Astronomical Society*, 436(3):2398–2411, 2013.

H. Baumgardt and M. Hilker. A catalogue of masses, structural parameters, and velocity dispersion profiles of 112 milky way globular clusters. *Monthly Notices of the Royal Astronomical Society*, 478(2):1520–1557, 2018.

A. Bellini, G. Piotto, L. Bedin, I. King, J. Anderson, A. Milone, and Y. Momany. Radial distribution of the multiple stellar populations in centauri. *Astronomy & Astrophysics*, 507(3):1393–1408, 2009.

A. Bellini, J. Anderson, L. Bedin, I. King, R. van der Marel, G. Piotto, and A. Cool. The state-of-the-art hst astro-photometric analysis of the core of ω centauri. i. the catalog. *The Astrophysical Journal*, 842(1):6, 2017.

A. Bellini, M. Libralato, L. R. Bedin, A. P. Milone, R. P. Van Der Marel, J. Anderson, D. Apai, A. J. Burgasser, A. F. Marino, and J. M. Rees. The hst large

programme on ω centauri. ii. internal kinematics. *The Astrophysical Journal*, 853 (1):86, 2018.

A. Brown, A. Vallenari, T. Prusti, J. De Bruijne, C. Babusiaux, C. Bailer-Jones, M. Biermann, D. W. Evans, L. Eyer, F. Jansen, et al. Gaia data release 2-summary of the contents and survey properties. *Astronomy & astrophysics*, 616: A1, 2018.

F. Castelli. Atlas12: how to use it. *Memorie della Societa Astronomica Italiana Supplementi*, 8:25, 2005.

G. Collaboration et al. The gaia mission. *arXiv preprint arXiv:1609.04153*, 2016.

M. J. Cordero, C. A. Pilachowski, C. I. Johnson, I. McDonald, A. A. Zijlstra, and J. Simmerer. Detailed abundances for a large sample of giant stars in the globular cluster 47 tucanae (ngc 104). *The Astrophysical Journal*, 780(1):94, 2013.

G. Cordoni, A. Milone, A. Mastrobuono-Battisti, A. Marino, E. Lagioia, and M. Tailo. Kinematics of multiple stellar populations in globular clusters with gaia. *Proceedings of the International Astronomical Union*, 14(S351):281–284, 2019.

P. A. Crowther, S. Caballero-Nieves, K. Bostroem, J. M. Apellániz, F. Schneider, N. Walborn, C. Angus, I. Brott, A. Bonanos, A. de Koter, et al. The r136 star cluster dissected with hubble space telescope/stis. i. far-ultraviolet spectroscopic census and the origin of he ii λ1640 in young star clusters. *Monthly Notices of the Royal Astronomical Society*, 458(1):624–659, 2016.

E. Dalessandro, A. Mucciarelli, M. Bellazzini, A. Sollima, E. Vesperini, J. Hong, V. Hénault-Brunet, F. Ferraro, R. Ibata, B. Lanzoni, et al. The unexpected kinematics of multiple populations in ngc 6362: do binaries play a role? *The Astrophysical Journal*, 864(1):33, 2018.

F. D'Antona, M. Di Criscienzo, T. Decressin, A. Milone, E. Vesperini, and P. Ventura. The extended main-sequence turn-off cluster ngc 1856: rotational evolution in a coeval stellar ensemble. *Monthly Notices of the Royal Astronomical Society*, 453(3):2637–2643, 2015.

S. De Mink, O. Pols, N. Langer, and R. Izzard. Massive binaries as the source of abundance anomalies in globular clusters. *Astronomy & Astrophysics*, 507(1): L1–L4, 2009.

P. Denissenkov and F. Hartwick. Supermassive stars as a source of abundance anomalies of proton-capture elements in globular clusters. *Monthly Notices of the Royal Astronomical Society*, 437(1):L21–L25, 2014.

P. Denissenkov, D. VandenBerg, F. Hartwick, F. Herwig, A. Weiss, and B. Paxton. The primordial and evolutionary abundance variations in globular-cluster stars: a problem with two unknowns. *Monthly Notices of the Royal Astronomical Society*, 448(4):3314–3324, 2015.

A. D'Ercole, F. D'Antona, P. Ventura, E. Vesperini, and S. L. McMillan. Abundance patterns of multiple populations in globular clusters: a chemical evolution model based on yields from agb ejecta. *Monthly Notices of the Royal Astronomical Society*, 407(2):854–869, 2010.

A. Dotter, B. Chaboyer, D. Jevremović, V. Kostov, E. Baron, and J. W. Ferguson. The dartmouth stellar evolution database. *The Astrophysical Journal Supplement Series*, 178(1):89, 2008.

A. Dotter, A. Sarajedini, J. Anderson, A. Aparicio, L. R. Bedin, B. Chaboyer, S. Majewski, A. Marín-Franch, A. Milone, N. Paust, et al. The acs survey of galactic globular clusters. ix. horizontal branch morphology and the second parameter phenomenon. *The Astrophysical Journal*, 708(1):698–716, 2010.

M. Gieles, C. Charbonnel, M. G. Krause, V. Hénault-Brunet, O. Agertz, H. J. Lamers, N. Bastian, A. Gualandris, A. Zocchi, and J. A. Petts. Concurrent formation of supermassive stars and globular clusters: implications for early self-enrichment. *Monthly Notices of the Royal Astronomical Society*, 478(2):2461–2479, 2018.

W. E. Harris. A catalog of parameters for globular clusters in the milky way. *The Astronomical Journal*, 112:1487, 1996.

M. Krause, C. Charbonnel, T. Decressin, G. Meynet, and N. Prantzos. Superbubble dynamics in globular cluster infancy-ii. consequences for secondary star formation in the context of self-enrichment via fast-rotating massive stars. *Astronomy & Astrophysics*, 552:A121, 2013.

R. L. Kurucz. Atlas12, synthe, atlas9, width9, et cetera. *Memorie della Societa Astronomica Italiana Supplementi*, 8:14, 2005.

J.-W. Lee. Multiple stellar populations of globular clusters from homogeneous ca-cn photometry. iv. toward precision populational tagging. *The Astrophysical Journal*, 872(1):41, 2019.

A. Marin-Franch, A. Aparicio, G. Piotto, A. Rosenberg, B. Chaboyer, A. Sarajedini, M. Siegel, J. Anderson, L. R. Bedin, A. Dotter, et al. The acs survey of galactic globular clusters. vii.* relative ages. *The Astrophysical Journal*, 694(2):1498, 2009.

A. Marino, A. Milone, A. Renzini, F. D'Antona, J. Anderson, L. Bedin, A. Bellini, G. Cordoni, E. Lagioia, G. Piotto, et al. The hubble space telescope uv legacy survey of galactic globular clusters–xix. a chemical tagging of the multiple stellar populations over the chromosome maps. *Monthly Notices of the Royal Astronomical Society*, 487(3):3815–3844, 2019a.

A. Marino, A. Milone, A. Sills, D. Yong, A. Renzini, L. Bedin, G. Cordoni, F. D'Antona, H. Jerjen, A. Karakas, et al. Chemical abundances along the 1g sequence of the chromosome maps: the globular cluster ngc 3201. *The Astrophysical Journal*, 887(1):91, 2019b.

F. Martins, J. Morin, C. Charbonnel, C. Lardo, and W. Chantereau. Impact of a companion and of chromospheric emission on the shape of chromosome maps for globular clusters. *Astronomy & Astrophysics*, 635:A52, 2020.

A. Milone, A. Marino, S. Cassisi, G. Piotto, L. Bedin, J. Anderson, F. Allard, A. Aparicio, A. Bellini, R. Buonanno, et al. The infrared eye of the wide-field camera 3 on the hubble space telescope reveals multiple main sequences of very low mass stars in ngc 2808. *The Astrophysical Journal Letters*, 754(2):L34, 2012a.

A. Milone, G. Piotto, L. Bedin, A. Aparicio, J. Anderson, A. Sarajedini, A. Marino, A. Moretti, M. B. Davies, B. Chaboyer, et al. The acs survey of galactic globular clusters-xii. photometric binaries along the main sequence. *Astronomy & Astrophysics*, 540:A16, 2012b.

A. Milone, G. Piotto, L. Bedin, I. King, J. Anderson, A. Marino, A. Bellini, R. Gratton, A. Renzini, P. Stetson, et al. Multiple stellar populations in 47 tucanae. *The Astrophysical Journal*, 744(1):58, 2012c.

A. Milone, A. Marino, G. Piotto, L. Bedin, J. Anderson, A. Aparicio, A. Bellini, S. Cassisi, F. D'Antona, F. Grundahl, et al. A wfc3/hst view of the three stellar populations in the globular cluster ngc 6752. *The Astrophysical Journal*, 767(2): 120, 2013.

A. Milone, A. Marino, L. Bedin, G. Piotto, S. Cassisi, A. Dieball, J. Anderson, H. Jerjen, M. Asplund, A. Bellini, et al. The m 4 core project with hst–ii. multiple stellar populations at the bottom of the main sequence. *Monthly Notices of the Royal Astronomical Society*, 439(2):1588–1595, 2014a.

A. Milone, A. Marino, A. Dotter, J. Norris, H. Jerjen, G. Piotto, S. Cassisi, L. Bedin, A. R. Blanco, A. Sarajedini, et al. Global and nonglobal parameters of horizontal-branch morphology of globular clusters. *The Astrophysical Journal*, 785(1):21, 2014b.

A. Milone, A. Marino, G. Piotto, L. Bedin, J. Anderson, A. Renzini, I. King, A. Bellini, T. Brown, S. Cassisi, et al. The hubble space telescope uv legacy survey of galactic globular clusters–ii. the seven stellar populations of ngc 7089 (m2). *Monthly Notices of the Royal Astronomical Society*, 447(1):927–938, 2015a.

A. Milone, A. Marino, G. Piotto, A. Renzini, L. Bedin, J. Anderson, S. Cassisi, F. D'Antona, A. Bellini, H. Jerjen, et al. The hubble space telescope uv legacy survey of galactic globular clusters. iii. a quintuple stellar population in ngc 2808. *The Astrophysical Journal*, 808(1):51, 2015b.

A. Milone, G. Piotto, A. Renzini, A. Marino, L. Bedin, E. Vesperini, F. D'Antona, D. Nardiello, J. Anderson, I. King, et al. The hubble space telescope uv legacy survey of galactic globular clusters–ix. the atlas of multiple stellar populations. *Monthly Notices of the Royal Astronomical Society*, 464(3):3636–3656, 2017.

A. Milone, A. Marino, A. Renzini, F. D'Antona, J. Anderson, B. Barbuy, L. Bedin, A. Bellini, T. Brown, S. Cassisi, et al. The hubble space telescope uv legacy survey of galactic globular clusters–xvi. the helium abundance of multiple populations. *Monthly Notices of the Royal Astronomical Society*, 481(4):5098–5122, 2018.

A. Milone, A. Marino, L. Bedin, J. Anderson, D. Apai, A. Bellini, A. Dieball, M. Salaris, M. Libralato, D. Nardiello, et al. The hst large programme on ngc 6752–ii. multiple populations at the bottom of the main sequence probed in nir. *Monthly Notices of the Royal Astronomical Society*, 484(3):4046–4053, 2019.

A. P. Milone. Thirteen facts that you need to know on multiple populations in globular clusters. *arXiv preprint arXiv:1908.11703*, 2019.

D. Nardiello, A. Milone, G. Piotto, A. Marino, A. Bellini, and S. Cassisi. Observing multiple stellar populations with vlt/fors2-main sequence photometry in outer regions of ngc 6752, ngc 6397, and ngc 6121 (m 4). *Astronomy & Astrophysics*, 573:A70, 2015.

H. B. Richer, J. Heyl, J. Anderson, J. S. Kalirai, M. M. Shara, A. Dotter, G. G. Fahlman, and R. M. Rich. A dynamical signature of multiple stellar populations in 47 tucanae. *The Astrophysical Journal Letters*, 771(1):L15, 2013.

M. Salaris and S. Cassisi. Lithium and oxygen in globular cluster dwarfs and the early disc accretion scenario. *Astronomy & Astrophysics*, 566:A109, 2014.

L. Sbordone. Kurucz's codes under gnu-linux. *arXiv preprint astro-ph/0509337*, 2005.

L. Sbordone, P. Bonifacio, and F. Castelli. Atlas 9 and atlas 12 under gnu-linux. *Proceedings of the International Astronomical Union*, 2(S239):71–73, 2007.

A. Sollima, F. Ferraro, M. Bellazzini, L. Origlia, O. Straniero, and E. Pancino. Deep fors1 observations of the double main sequence of ω centauri. *The Astrophysical Journal*, 654(2):915, 2007.

M. Tailo, F. D'Antona, V. Caloi, A. Milone, A. Marino, E. Lagioia, and G. Cordoni. Is helium the key parameter in the extended colour spread of the first generation stars in m3? *Monthly Notices of the Royal Astronomical Society*, 486(4):5895–5906, 2019.

M. Tailo, A. Milone, E. Lagioia, F. D'Antona, A. Marino, E. Vesperini, V. Caloi, P. Ventura, E. Dondoglio, and G. Cordoni. Mass-loss along the red giant branch in 46 globular clusters and their multiple populations. *Monthly Notices of the Royal Astronomical Society*, 498(4):5745–5771, 2020.

D. A. VandenBerg, K. Brogaard, R. Leaman, and L. Casagrande. The ages of 55 globular clusters as determined using an improved method along with color-magnitude diagram constraints, and their implications for broader issues. *The Astrophysical Journal*, 775(2):134, 2013.

P. Ventura, M. Di Criscienzo, R. Carini, and F. D'Antona. Yields of agb and sagb models with chemistry of low-and high-metallicity globular clusters. *Monthly Notices of the Royal Astronomical Society*, 431(4):3642–3653, 2013.

D. Yong, F. Grundahl, J. A. Johnson, and M. Asplund. Nitrogen abundances in giant stars of the globular cluster ngc 6752. *The Astrophysical Journal*, 684(2): 1159, 2008.

M. Zennaro, A. Milone, A. Marino, G. Cordoni, E. Lagioia, and M. Tailo. Four stellar populations and extreme helium variation in the massive outer-halo globular cluster ngc 2419. *Monthly Notices of the Royal Astronomical Society*, 487 (3):3239–3251, 2019.